MEASUREMENT SCIENCE REVIEW, **18**, (2018), No. 1, 1–6

DE GRUYTER OPEN

MEASUREMENT SCIENCE REVIEW

Journal homepage: http://www.degruyter.com/view/j/msr

ISSN 1335-8871

Time Alignment as a Necessary Step in the Analysis of Sleep Probabilistic Curves

Zuzana Rošťáková[1,2], Roman Rosipal[1]

[1]*Institute of Measurement Science, Slovak Academy of Sciences, Dúbravská cesta 9, 841 04 Bratislava, Slovakia, zuzana.rostakova@savba.sk*

[2]*Faculty of Electrical Engineering and Information Technology, Slovak University of Technology, Ilkovičova 3, 812 19 Bratislava, Slovakia*

Sleep can be characterised as a dynamic process that has a finite set of sleep stages during the night. The standard Rechtschaffen and Kales sleep model produces discrete representation of sleep and does not take into account its dynamic structure. In contrast, the continuous sleep representation provided by the probabilistic sleep model accounts for the dynamics of the sleep process. However, analysis of the sleep probabilistic curves is problematic when time misalignment is present. In this study, we highlight the necessity of curve synchronisation before further analysis. Original and in time aligned sleep probabilistic curves were transformed into a finite dimensional vector space, and their ability to predict subjects' age or daily measures is evaluated. We conclude that curve alignment significantly improves the prediction of the daily measures, especially in the case of the *S2*-related sleep states or slow wave sleep.

Keywords: Curve alignment, probabilistic sleep model, functional principal component analysis.

1. Introduction

Sleep is a continuous process that can be described by a finite number of sleep stages. The Rechtschaffen and Kales sleep model (R&K) [1] distinguishes five basic sleep stages. These include the *Wake* stage, or stage of full wakefulness; stages *S1* (light sleep), *S2*, *S3*, and *S4*, also called *nonREM* stages; and finally, the *REM* (rapid eye movement) stage, during which quick eye movements behind closed eyelids are typical. Stages *S3* and *S4* represent slow wave sleep *SWS* (or deep sleep), and in this study are considered together. The R&K model is mainly based on the analysis of EEG signals, which are divided into non-overlapping 30-second segments; each time segment is assigned to one of the above-mentioned sleep stages. This results in a discrete sleep representation known as a sleep hypnogram, where changes between a small number of sleep stages are not smooth.

The probabilistic sleep model (PSM) [2] is an alternative method of sleep process modelling. The model is EEG-based, but in contrast to the R&K model, only 3-second time segments are considered, and PSM distinguishes 20 sleep states called sleep microstates. Instead of strict assignment of a time segment to one of the 20 sleep states, a probability value is computed for each sleep microstate separately. Considering the probability values as a function of time, a sleep probabilistic curve is obtained (Fig. 1).

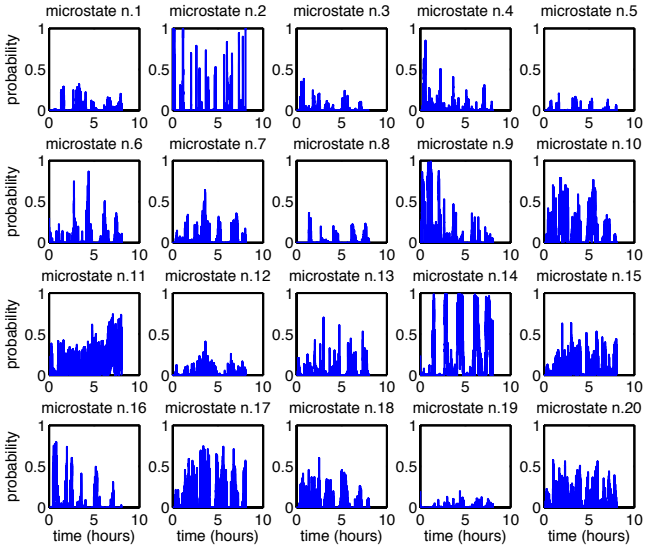

Fig. 1. An example of sleep probabilistic curves for 20 sleep microstates. The blue curves represent a whole night profile of a 42-year-old healthy man.

DOI: 10.1515/msr-2018-0001

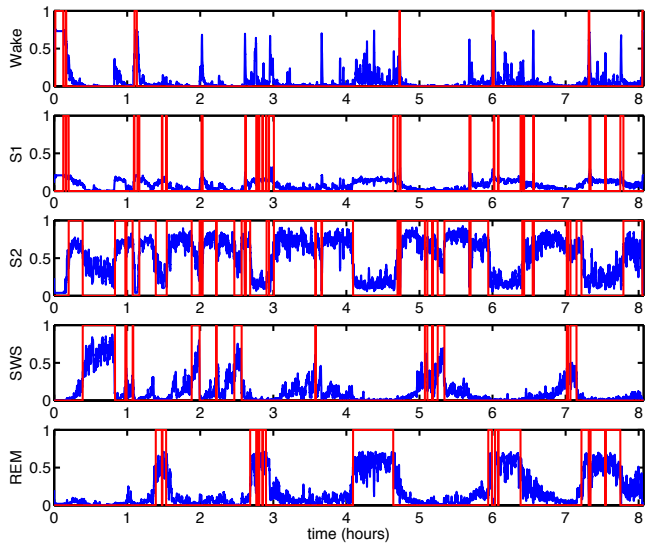

Fig.2. An example of the sleep probabilistic curves for sleep stages *Wake, S1, S2, SWS, REM*. The blue curves represent a whole night profile of a 42-year-old healthy man. Corresponding Rechtschaffen and Kales scores [1] are depicted in red.

Physiological interpretation of sleep microstates is not straightforward. Therefore, PSM also estimates the probability (weights) of similarities between microstates and the standard sleep stages *Wake, S1, S2, SWS* or *REM*. For example, using the current analysis, sleep microstate 1 is similar to the *S2* stage, with the probability of 84.7%, and to the *REM* stage with the probability of 10.9%. Thus, the sum of probabilities to the other R&K sleep stages is 4.4%.

In addition to the interpretation of sleep microstates, estimated probabilities may be used as weights in a linear combination of the sleep microstates in order to reconstruct probabilistic curves for the standard R&K sleep stages (Fig. 2). In the analysis of the sleep probabilistic curves, we aimed to find typical overnight sleep profiles which significantly correlated with age or daily life performance. However, when the curves are misaligned in time (Fig. 3), the relationship with daily life measures is difficult to detect. Two curves X and Y observed on the approximately same time interval $T = [a,b]$ are misaligned if they are of similar shape, but important features like local maxima or minima are shifted in time.

To align a pair of curves X,Y means to find a strictly increasing time transformation $h : T \to T$ which minimises chosen similarity criterion C between the curves under the assumption of the common start and end point

$$h(a) = a \quad \text{and} \quad h(b) = b.$$

The area under the squared difference of two curves

$$C(X, Y \circ h) = \int_T (X(t) - Y \circ h(t))^2 \, dt \qquad (1)$$

is an example of a similarity criterion which is used with small modifications in the majority of the curve alignment methods.

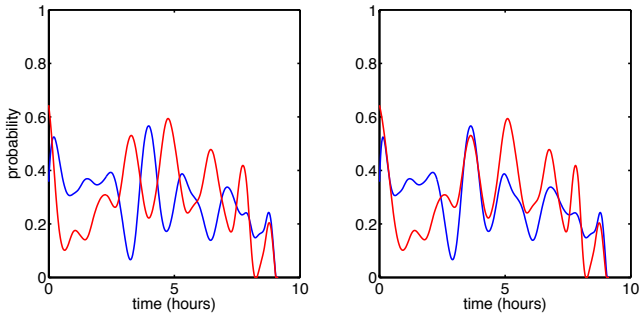

Fig.3. An example of two smoothed sleep probabilistic curves with similar overnight profiles misaligned in time (left), and the aligned version (right).

Two of the many methods developed for curve alignment are self-modelling time warping [3] and pairwise curve synchronisation [4]. The first method aligns a set of curves to one common target curve, while the second approach aligns each pair of curves separately. The curve alignment by moments [5] defines a set of moments in a curve and aligns two curves in such a way that the difference between their moments is as small as possible. Following our previous practical experience with the presented sleep dataset, we prefer the elastic time warping method as described in [6]. The general idea of elastic warping was first mentioned in [7] or [8]. This method aligns transformations of each curve called the *square-root slope function* by using the criterion (1), rather than curves themselves. For more detail, see [6].

There may exist sleep features in which exact timing influences sleep quality and daily behaviour. Therefore, we aimed to detect sleep microstates or standard sleep stages where the time alignment of the sleep probabilistic curves significantly improves correlations between the sleep structure and daily measures, and conversely, where the curve alignment is counter-productive.

2. Subject and Methods

In this study, the polysomnographic (PSG) recordings of 146 healthy subjects spending two consecutive nights in the sleep laboratory were used. These recordings represent a subset of PSG data collected in the European sleep project SIESTA [9].

After awakening, the subjects participated in a battery of neuropsychological tests. They were also asked to subjectively score their sleep quality or level of drive and drowsiness [10]. In addition, in the morning and evening, their pulse rate and blood pressure were recorded. The whole set of daily measures collected is listed in Table 1.

In addition to the original daily measures, we considered three artificial factors – factor of subjectively scored sleep quality (FA1), physiological factor (FA2), and neuropsychological factor (FA3). These factors were obtained by applying the factor analysis method to the set of all available daily measures [10].

Table 1. The list of daily measures and their abbreviations used in the article. For more details about the cognitive tests or questionnaires see [10].

Abbreviation	Measure
s_qua	subjectively scored sleep quality
a_qua	subjectively scored awakening quality
s_com	subjectively scored somatic complaints
wb_m, wb_e	well-being morning/evening
drive	level of drive in the morning
drows	level of drowsiness in the morning
aff	level of affectivity in the morning
mood	level of mood in the morning
pul_m, pul_e	pulse rate in the morning/evening
dia_m, dia_e	diastolic blood pressure in the morning/evening
sys_m, sys_e	systolic blood pressure in the morning/evening
num_m	numerical memory test
ad_ts	alphabetical cross-out test, total score
ad_sv	alphabetical cross-out test, attention variability
errp	alphabetical cross-out test, percentage of errors
fma_r, fma_l	fine motor activity test (right and left hand)

First, PSM was applied to the PSG data, and sleep probabilistic curves of 20 sleep microstates were extracted. Because of a high time variation between the beginning of sleep (lights off) and falling asleep, the beginning of all probabilistic sleep curves was set to the sleep latency, which is defined as three consecutive 30-second periods of the *S1* stage, or the first period of the *S2* stage, whichever comes first.

In the second step the probabilistic curves for the standard sleep stages *Wake, S1, S2, SWS* or *REM* were reconstructed by using the sleep probabilistic curves of 20 sleep microstates, and similarity weights estimated by the PSM.

The sleep probabilistic curves were smoothed by applying the functional principal component analysis (FPCA) method with smoothing covariance surface [11]. The smoothing step and the procedure described below were performed for each sleep microstate or standard sleep stage separately.

The FPCA method is also able to predict the sleep probabilistic curves profile at the end of the night according to the behaviour of the whole database. Therefore, we can define curves of all subjects over the same time interval.

A by-product of the FPCA method is the transformation of a functional half-space of all non-negative curves into a finite dimensional vector space of principal component scores. Each smoothed sleep probabilistic curve $X_i,\ i = 1,\ldots,N$ where $N = 2 \times 146 = 292$ can be expressed as a sum of an overall mean curve μ and a linear combination of K functional principal components $\phi_1,\ldots,\phi_K$

$$X_i(t) = \mu(t) + \sum_{j=1}^{K} a_{ij}\phi_j(t). \tag{2}$$

Functions $\phi_j : T \to \mathbb{R},\ j = 1,\ldots,K$ are normalised and mutually orthogonal

$$\int_T \phi_i(t)\phi_j(t)dt = \begin{cases} 0, & i \neq j, \\ 1, & i = j. \end{cases}$$

The vector of principal component scores

$$a_i = (a_{i1},\ldots,a_{iK})^T, \qquad i = 1,\ldots,N$$

was used for further analysis, as the representative of the curve X_i.

To relate principal component scores of the sleep probabilistic curves with daily measures, a linear regression model was applied. For a chosen sleep state, the dataset was divided into a training and a testing part. A daily measure m was modelled as a linear combination of principal component scores belonging to the training dataset D_{train}

$$m_i = \beta_0 + \sum_{j=1}^{K} \beta_j a_{ij} + \varepsilon_i, \qquad i \in D_{train},$$

where the estimators $\widehat{\beta_0},\ldots,\widehat{\beta_K}$ for the unknown parameters were obtained by the standard method of least squares. Then we tested whether the estimated model is significantly better than a constant model. After that, values of the daily measure for the testing dataset D_{test} were predicted by the estimated linear model

$$\widehat{m_l} = \widehat{\beta_0} + \sum_{j=1}^{K} \widehat{\beta_j} a_{lj}, \qquad l \in D_{test}.$$

Finally, Spearman's correlation coefficient was computed between real values $m_l,\ l \in D_{test}$ and predicted values $\widehat{m_l},\ l \in D_{test}$.

To avoid misinterpretation of results caused by random splitting into training and testing datasets, 10-fold cross-validation was considered.

In the next step, the sleep probabilistic curves were aligned in time by the elastic time warping method [6] immediately after smoothing. The alignment was carried out for each sleep state separately. Transformation of aligned curves into principal component scores and modelling of daily measures were done in the same way as described above. Finally, the Wilcoxon test was performed to detect whether the difference between correlation coefficients obtained from the original and aligned curves was significant.

Different division of the data into 10 folds may lead to slightly different results. Therefore, the whole procedure was repeated 100 times and differences in correlations based on misaligned or aligned curves were considered as significant if the Wilcoxon test rejected the null hypothesis (no difference between correlation coefficients) in more than 40 trials.

3. Results

3.1. Sleep microstates

Time synchronisation of the sleep probabilistic curves of 20 sleep microstates resulted in a few changes of correlations between real and predicted values of daily measures (Table 2).

Table 2. Average correlation coefficients for daily measures and sleep microstates. Only results where a significant difference between original and aligned curves was detected by the Wilcoxon test are presented. The percentage of linear models which were significantly better than a constant model is depicted in brackets.

Daily meas.	Microstate	p-value	$\bar{\rho}$, misaligned curves		$\bar{\rho}$, aligned curves	
wb_m	5 (65% SWS)	0.011	−0.14	(0%)	**0.10**	(91%)
aff	8 (73% REM)	0.017	0.02	(0%)	**0.13**	(37%)
	9 (76% S2)	0.017	−0.04	(7%)	**0.16**	(94%)
	19 (88% W)	0.014	−0.13	(0%)	**0.09**	(0%)
FA2	14 (72% REM)	0.021	**0.25**	(54%)	0.10	(0%)
	20 (63% S2)	0.014	0.05	(9%)	**0.25**	(100%)
pul_m	8 (73% REM)	0.038	0.02	(2%)	**0.17**	(99%)
sys_m	14 (72% REM)	0.054	**0.21**	(100%)	0.03	(0%)
dia_m	14 (72% REM)	0.021	**0.15**	(69%)	−0.02	(0%)
dia_e	1 (85% S2)	0.045	−0.08	(0%)	**0.13**	(87%)
FA3	6 (85% Wake)	0.017	**0.25**	(99%)	0.05	(11%)
	8 (73% REM)	0.054	0.02	(0%)	**0.17**	(80%)
ad_sv	5 (65% SWS)	0.001	−0.13	(0%)	**0.14**	(63%)

In the case of subjectively scored sleep and awakening quality, the only significant difference was observed in the case of morning well-being (*wb_m*) and affectivity (*aff*) tests.

The sleep microstate 5 represents deeper sleep (65 % *SWS*, 35% *S2*) and the principal component scores of the original, in time misaligned sleep probabilistic curves, were not able to predict the values of *wb_m*. An increment in average correlation values was observed after curve alignment, and the percentage of linear models being significantly better than a constant model was higher (0% for misaligned curves and 91% for aligned curves).

The average correlations between the real level of affectivity in the morning and its values predicted by using principal component scores of misaligned curves corresponding either to microstate 8 (73% *REM*) or 19 (88% *Wake*) were close to zero, and none of the fitted models was better than a constant model. Thus, it was impossible to predict the level of affectivity by using the information from these microstates. After curve alignment, the average correlations increased in both cases, but were still low, see Table 2. Improvement in percentage of linear models being significantly better than a constant model was observed only in the case of microstate 8.

No relationship between the structure of the sleep microstate 9 (76% *S2*) and the level of affectivity in the morning was detected when misaligned sleep probabilistic curves were used. The average correlation was $\bar{\rho} = -0.04$ and the ratio of trained linear models which outperformed a constant model was less than 10% (Table 2). In contrast, after curve alignment, the average correlation increased to 0.16, and the percentage of linear models being significantly better than a constant model was also higher.

Considering the physiological measures, the curve alignment produced significant changes in correlations, especially in *REM*-related sleep microstate 14. The average correlations between the real and predicted values of FA2, systolic and diastolic pressure in the morning decreased after curve alignment (Table 2). The ratio of linear models outperforming a constant model was equal to 0. However, for the misaligned cases, the percentage was above 50% in all three cases. This indicates that curve alignment is counterproductive for microstate 14.

Microstate 8 is also similar to the *REM* stage, but its characteristics differ from those of microstate 14. As depicted in Table 2, the average correlations with pulse rate in the morning changed from insignificant for in time misaligned curves to significant (≈ 0.17) after the curves were aligned. The curve alignment also increased the percentage of linear models outperforming a constant model (99 %), indicating that there may exist a relationship between the structure of microstate 8 and the pulse rate in the morning.

The last difference was observed in the case of the *S2*-related sleep microstates 1 and 20 (Table 2) and FA2 or diastolic blood pressure in the evening. In both cases, curve alignment produced higher correlations in contrast to the case of misaligned curves. The percentage of linear models being better than a constant model was above 87% after curve alignment.

Significant average correlations (≈ 0.25) between the FA3 factor score and the structure of the microstate 6 diminished after curve alignment. This microstate characterises full awakening during the night or in the morning. The amount of time spent awake during the night influences our cognitive performance in the morning. However, after curve alignment the information about the exact amount of time spent awake is missing, and therefore, a decrement in average correlation values and in the percentage of linear models better than a constant model was observed.

For FA3 or *ad_sv* the curve alignment improved the prediction ability of linear models fitted to the principal component scores of either microstate 8 (73% *REM*) or 5 (65% *SWS*). In addition, the percentage of linear models outperforming a null model increased after curve alignment from 0% for misaligned curves to 80% for microstate 8 or 63% for microstate 5. However, the difference between average correlations produced by either misaligned or aligned curves of microstate 8 was at the edge of significance (p-value = 0.054).

3.2. Standard R&K sleep stages

The alignment of the sleep probabilistic curves caused changes in correlations between real and predicted results of daily measures, especially for the *REM* stage (Table 3).

Improvement was observed in the case of age, physiological factors, or the results of the numerical memory test. In the last case, the insignificant correlation between daily measures and misaligned curves became statistically significant after curve alignment. Moreover, the percentage of linear models which were significantly better than a constant model increased from 0% for misaligned curves to 85% for aligned curves.

In the case of the level of mood or affectivity, the average correlations between real and predicted values were significantly lower for aligned curves for the *REM* stage. However, no estimated linear model was better than a constant model

Table 3. Average correlation coefficients for daily measures and sleep stages. The same notation as in Table 2 is used.

Daily meas.	Sleep stage	p-value	$\bar{\rho}$ misaligned curves	$\bar{\rho}$ aligned curves
age	REM	0.026	0.40 (100%)	**0.58** (100%)
drive	Wake	0.021	**0.14** (60%)	−0.05 (0%)
mood	REM	0.006	**0.02** (0%)	−0.23 (0%)
aff	REM	0.003	**0.01** (0%)	−0.22 (0%)
	S2	0.021	0.03 (8%)	**0.24** (100%)
FA2	REM	0.021	0.23 (83.2%)	**0.42** (100%)
num_m	REM	0.014	−0.03 (0%)	**0.13** (85%)

for either aligned or misaligned curves. We hypothesize that the relationship between the *REM* stage and the level of mood or affectivity simply does not exist, or we are not able to detect it either with original or in time aligned curves.

For the *Wake* stage, the only significant change observed was a decreased correlation with the level of drive in the aligned curves. More than half of the linear models were significantly better than a constant model when using principal component scores of the misaligned curves. This indicates the existence of a relationship between the *Wake* stage profile and the level of drive. However, after alignment, this relationship disappeared (the percentage was exactly 0).

Regarding the sleep stages *S1, S2* or *SWS*, the correlations between real and predicted values of daily measures were higher for aligned curves in several cases, but not significantly.

4. Discussion and Conclusions

In this study, we demonstrated the benefit of time alignment of sleep probabilistic curves when detecting the relationship between sleep structure and daily measures. The sleep probabilistic curves of either 20 sleep microstates or five standard sleep stages were aligned using the elastic warping method.

The improvement in average correlations between real and predicted values of daily measures was observed after curve alignment in the *S2*- and *SWS*-related sleep microstates, which is consistent with the results observed in the case of the standard sleep stages. We can conclude that the whole structure of the sleep states related to the *S2* stage or SWS is more important than the exact timing of their periods.

The PSM distinguishes two sleep microstates similar to the *REM* stage. In the case of microstate 8 (73% *REM*), curve alignment helps to detect existing relationships between the structure of the microstate and morning pulse rate or level of affectivity. However, alignment of the sleep probabilistic curves of microstate 14 (72% *REM*) led to a decrement in average correlations. When considering the standard *REM* stage, new or improved correlations with daily measures were observed after curve alignment. The benefit of curve alignment for the *REM* stage is therefore questionable. We recommend the use of both misaligned and aligned versions of sleep probabilistic curves of microstates similar to the *REM* stage, and careful interpretation of the results.

These results indicate different structures of the two *REM*-related sleep microstates and confirm the necessity of a larger set of sleep states considered by PSM, in contrast to the standard R&K model.

Considering either aligned sleep probabilistic curves of the *Wake* stage or sleep microstates related to wakefulness, the average correlations were significantly lower in comparison to the misaligned case. Moreover, the percentage of linear models outperforming a constant model decreased. We hypothesize that, for the *Wake* stage, the exact timing of sleep features is important for the sleep quality and cognitive performance in the morning.

Finally, we can conclude that curve alignment is useful as a pre-processing step, especially when analysing the structure of *S2*, *SWS*, or related microstates.

Acknowledgement

This research was supported by the Slovak Research and Development Agency (grants number APVV-0668-12 and APVV-16-0202) and by the VEGA 2/0011/16 grant.

References

[1] Rechtschaffen, A., Kales, A. (1968). *A Manual of Standardized Terminology Techniques and Scoring System for Sleep Stages of Human Subjects*. Public Health Service, U.S. Government Printing Office, Washington, D.C.

[2] Lewandowski, A., Rosipal, R., Dorffner, G. (2012). Extracting more information from EEG recordings for a better description of sleep. *Computer Method and Programs in Biomedicine*, 108 (3), 961–972.

[3] Gervini, D., Gasser, T. (2004). Self-modeling warping functions. *Journal of the Royal Statistical Society: Series B (Statistical Methodology)*, 66 (4), 959–971.

[4] Müller, H. G., Tang, R. (2008). Pairwise curve synchronisation for functional data. *Biometrika*, 95 (4), 875–889.

[5] James, G.M. (2007). Curve alignment by moments. *The Annals of Applied Statistics*, 1 (2), 480–501.

[6] Tucker, J.D., Wu, W., Srivastava, A. (2013). Generative models for functional data using phase and amplitude separation. *Computational Statistics and Data Analysis*, 61, 50–60.

[7] Srivastava, A., Klassen, E., Joshi, S.H., Jermyn, I.H. (2011). Shape analysis of elastic curves in euclidean spaces. *IEEE Transactions on Pattern Analysis and Machine Intelligence*, 33 (7), 1415–1428.

[8] Srivastava, A., Wu, W., Kurtek, S., Klassen, E., Marron, J. S. (2011). Registration of functional data using Fisher-Rao metric. *arXiv:*1103.3817 [math.ST].

[9] Klösch, G., Kemp, B., Penzel, T., Schlögl, A., Rappelsberger, P., Trenker, E., Gruber, G., Zeitlhofer, J., Saletu, B., Herrmann, W., Himanen, S., Kunz, D., Barbanoj, M., Röschke, J., Varri, A., Dorffner, G. (2001). The SIESTA project polygraphic and clinical database. *Medicine and Biology Magazine*, 20 (3), 51–57.

[10] Rosipal, R., Lewandowski, A., Dorffner, G. (2013). In search of objective components for sleep quality indexing in normal sleep. *Biological Psychology*, 94 (1), 210–220.

[11] Yao, F., Müller, H. G., Clifford, A. J., Dueker, S. R., Follet, J., Lin, Y., Buchholz, B. A., Vogel, J. S. (2003). Shrinkage estimation for functional principal component scores, with application to population kinetics of plasma folate. *Biometrics*, 59 (3), 676–685.

Received September 9, 2017.
Accepted February 12, 2018.

MEASUREMENT SCIENCE REVIEW, **18**, (2018), No. 1, 7-12

DE GRUYTER OPEN

MEASUREMENT SCIENCE REVIEW

Journal homepage: http://www.degruyter.com/view/j/msr

ISSN 1335-8871

I-cored Coil Probe Located Above a Conductive Plate with a Surface Hole

Grzegorz Tytko, Leszek Dziczkowski

Institute of Electronics, Faculty of Automatic Control, Electronics and Computer Science, The Silesian University of Technology, Akademicka 16, 44-100, Gliwice, Poland, grzegorz.tytko@polsl.pl

This work presents an axially symmetric mathematical model of an I-cored coil placed over a two-layered conductive material with a cylindrical surface hole. The problem was divided into regions for which the magnetic vector potential of a filamentary coil was established applying the truncated region eigenfunction expansion method. Then the final formula was developed to calculate impedance changes for a cylindrical coil with reference to both the air and to a material with no hole. The influence of a surface flaw in the conductive material on the components of coil impedance was examined. Calculations were made in Matlab for a hole with various radii and the results thereof were verified with the finite element method in COMSOL Multiphysics package. Very good consistency was achieved in all cases.

Keywords: Nondestructive testing, eddy current, coil impedance, calculation, modeling, truncated region eigenfunction expansion.

1. INTRODUCTION

Eddy current testing is used in many industries to detect defects in conductive materials. In view of a minor penetration depth of eddy currents to the workpiece, the highest effectiveness is achieved for shallow flaws existing in non-ferromagnetic materials. Such flaws may occur both during the production process and because of material cracking or corrosion.

The solution to the problem of an air-cored coil located over the conductive material with a flaw was achieved for the hole in a plate [1], surface hole in a half-space [2]-[3], slot in a plate [4], and a plate with two flaws [5]. These studies were performed using the truncated region eigenfunction expansion (TREE) method, which was also applied for derivation of mathematical models of a planar spiral coil [6], an I-cored coil [7]-[8], a pot core coil [9], and a grating eddy current displacement sensor (GECDS) [10]. The examinations are usually conducted for coils wound around a core since such models feature a much higher sensitivity. The instruments used by the authors included also probes designed as I-cored coils with an air gap situated along the core axis (Fig.1.), which is described in [11]. This paper presents a mathematical model of such an I-cored coil placed over a two-layered conductive material with a cylindrical surface hole.

The rectangular cross-section coil is shown in Fig.2. The solution domain was limited to the value of parameter *b*, while maintaining the continuity of a magnetic vector potential. At the same time, satisfying the boundary condition, $A_\varphi(r, z) = 0$ for $r = 0$ and $r = b$ was ensured. During the analysis a filamentary coil was used, for which expressions that describe the magnetic vector potential were derived. Closed-form expressions for the change of I-cored coil impedance were obtained both in relation to the air as well as to the material with no hole. The results achieved using the TREE method were verified with the finite element method (FEM), which showed a very good agreement.

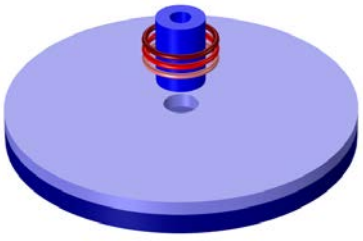

Fig.1. I-cored coil with a circular air gap inside the core column located above a conductive material with a surface hole.

2. SOLUTION

At first, the analysis included a filamentary coil with a core located over a two-layer conductive material with a hole, which is presented in Fig.3. The axially symmetric system was divided into 6 regions. For each region, a magnetic vector potential was obtained, which was written using the matrix notation.

DOI: 10.1515/msr-2018-0002

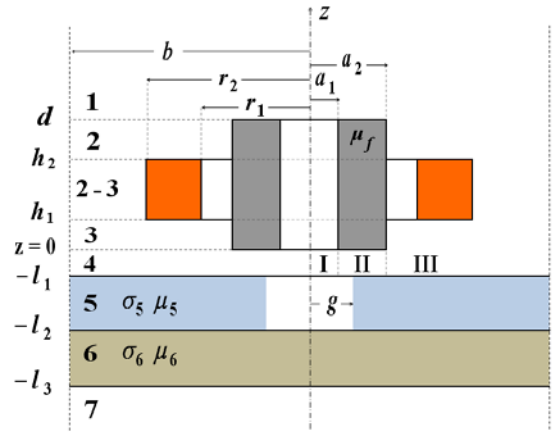

Fig.2. Rectangular cross-sectional coil located above a two-layered conductive plate with a hole.

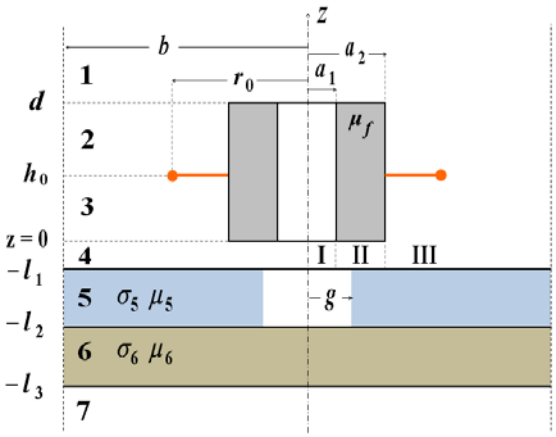

Fig.3. Filamentary coil located above a two-layered conductive plate with a hole.

$$\mathrm{A}_1(r,z) = J_1(\mathbf{q}^{\mathbf{T}} r)\ \mathbf{q}^{-1} e^{-\mathbf{q}z}\mathbf{C}_1 \tag{1}$$

$$\mathrm{A}_2(r,z) = \begin{matrix} J_1(\mathbf{m}^{\mathbf{T}} r) \\ L_1(\mathbf{m}^{\mathbf{T}} r) \\ L_1'(\mathbf{m}^{\mathbf{T}} r) \end{matrix} \mathbf{m}^{-1}(e^{-\mathbf{m}z}\mathbf{C}_2 - e^{\mathbf{m}z}\mathbf{B}_2) \quad \begin{matrix} 0 \le r \le a_1 \\ a_1 \le r \le a_2 \\ a_2 \le r \le b \end{matrix} \tag{2}$$

$$\mathrm{A}_3(r,z) = \begin{matrix} J_1(\mathbf{m}^{\mathbf{T}} r) \\ L_1(\mathbf{m}^{\mathbf{T}} r) \\ L_1'(\mathbf{m}^{\mathbf{T}} r) \end{matrix} \mathbf{m}^{-1}(e^{-\mathbf{m}z}\mathbf{C}_3 - e^{\mathbf{m}z}\mathbf{B}_3) \quad \begin{matrix} 0 \le r \le a_1 \\ a_1 \le r \le a_2 \\ a_2 \le r \le b \end{matrix} \tag{3}$$

$$\mathrm{A}_4(r,z) = J_1(\mathbf{q}^{\mathbf{T}} r)\ \mathbf{q}^{-1}(e^{-\mathbf{q}z}\mathbf{C}_4 - e^{\mathbf{q}z}\mathbf{B}_4) \tag{4}$$

$$\mathrm{A}_5(r,z) = \begin{matrix} J_1(\mathbf{u}^{\mathbf{T}} r) R_1(\mathbf{v}\, g) \\ R_1(\mathbf{v}^{\mathbf{T}} r) J_1(\mathbf{u}\, g) \end{matrix} \mathbf{u}^{-1}(e^{-\mathbf{u}z}\mathbf{C}_5 - e^{\mathbf{u}z}\mathbf{B}_5) \quad \begin{matrix} 0 \le r \le g \\ g \le r \le b \end{matrix} \tag{5}$$

$$\mathrm{A}_6(r,z) = J_1(\mathbf{q}^{\mathbf{T}} r)\ \mathbf{s}_6^{-1}(e^{-\mathbf{s}_6 z}\mathbf{C}_6 - e^{\mathbf{s}_6 z}\mathbf{B}_6) \tag{6}$$

$$\mathrm{A}_7(r,z) = -J_1(\mathbf{q}^{\mathbf{T}} r)\ \mathbf{q}^{-1} e^{\mathbf{q}z}\mathbf{B}_7 \tag{7}$$

where

$$\mathbf{u} = \sqrt{\mathbf{v}^2 + j\omega\mu_5\mu_0\sigma_5} \tag{8}$$

$$\mathbf{s}_6 = \sqrt{\mathbf{q}^2 + j\omega\mu_6\mu_0\sigma_6} \tag{9}$$

$J_1(\mathbf{q}^{\mathbf{T}} r),\ L_1(\mathbf{q}^{\mathbf{T}} r),\ L_1'(\mathbf{q}^{\mathbf{T}} r),\ J_1(\mathbf{u}^{\mathbf{T}} r), R_1(\mathbf{v}^{\mathbf{T}} r)$ – row vectors

$\mathbf{q}, \mathbf{m}, \mathbf{u}, \mathbf{v}, \mathbf{s}_6, e^{\pm\mathbf{q}z}, e^{\pm\mathbf{m}z}, e^{\pm\mathbf{u}z}, e^{\pm\mathbf{s}_6 z}$ – diagonal matrices

$\mathbf{C}_i, \mathbf{B}_i$ – column vectors of unknown coefficients

Discrete eigenvalues q_i and m_i are the positive roots of the equations (10) and (11). Such values are not present in region 5 that has a hole, so they are calculated in the same way as in the case of an I-cored coil located over the material without a hole [9].

$$J_1(q_i b) = 0 \qquad i = 0,1,2 \ldots Ns \tag{10}$$

$$L_1'(m_i b) = 0 \qquad i = 0,1,2 \ldots Ns \tag{11}$$

where

$$L_1'(m_i r) = B_{2F}'\, J_1(m_i r) + C_{2F}'\, Y_1(m_i r) \tag{12}$$

$$C_{2F}' = \frac{\pi}{2} m_i a_2 \left[\frac{J_1(m_i a_2) L_0(m_i a_2)}{\mu_f} - J_0(m_i a_2) L_1(m_i a_2)\right] \tag{13}$$

$$B_{2F}' = -\frac{\pi}{2} m_i a_2 \left[\frac{Y_1(m_i a_2) L_0(m_i a_2)}{\mu_f} - Y_0(m_i a_2) L_1(m_i a_2)\right] \tag{14}$$

$$L_n(m_i r) = B_{2F}\, J_n(m_i r) + C_{2F}\, Y_n(m_i r) \tag{15}$$

$$C_{2F} = \frac{\pi}{2} m_i a_1 (\mu_f - 1) J_0(m_i a_1) J_1(m_i a_1) \tag{16}$$

$$B_{2F} = \frac{\pi}{2} m_i a_1 [\mu_f J_0(m_i a_1) Y_1(m_i a_1) - J_1(m_i a_1) Y_0(m_i a_1)] \tag{17}$$

Region 5 of the analyzed problem consists of two sub-regions: air space (0 ≥ r ≥ g) and a conductive material (g ≥ r ≥ b). The magnetic vector potential for those sub-regions may be expressed in a general form as:

$$A_I = A_E\, J_1(u_i r) R_1(v_i g) \qquad 0 \le r \le g \tag{18}$$

$$A_{II} = A_E\, R_1(v_i\, r)\, J_1(u_i\, g) \qquad g \le r \le b \tag{19}$$

where

$$R_n(v_i\, x) = Y_1(v_i\, b)\, J_n(v_i\, x) + J_1(v_i\, b)\, Y_n(v_i\, x) \tag{20}$$

Equation (21) was obtained using the interface condition $(1/r)[\partial(rA)/\partial r] = 0$ in the radial direction for $r = g$ [7].

$$u_i\, R_1(v_i\, g)\, J_0(u_i\, g) = \frac{1}{\mu_5} v_i\, J_1(u_i\, g)\, R_0(v_i\, g) \tag{21}$$

Calculation of u_i and v_i eigenvalues is reduced to finding complex roots of the equation (21). Using numerical procedures, such as FindRoot() in Mathematica or fzero() in Matlab, requires providing initial values around which the roots are located. Such initial values may be taken as u_i values obtained upon the assumption that region 5 consists only of a conductive material or only of air. In the first case, when $g = 0$, we obtain $u_i = s_{5i}$, and in the second case $g = b$ and, in consequence, $u_i = q_i$ [7]. Unfortunately, this method may lead to omission of some roots. Higher effectiveness is achieved with the Newton-Raphson technique. However, in some cases even applying a very low increase in the argument does not ensure finding all the roots. The solution to this problem may be found by using more complex algorithms [10]-[11] which, upon appropriate selection of parameters, allow to properly derive all u_i, v_i values.

The unknown coefficients $\mathbf{C}_i$, $\mathbf{B}_i$ occurring in (1)-(7) were calculated using, for mutually neighboring regions of the problem, the following continuity conditions B_r and H_z.

$$A_i(r, z) = A_{i+1}(r, z) \tag{22}$$

$$\frac{1}{\mu_i}\frac{\partial A_i}{\partial z} - \frac{1}{\mu_{i+1}}\frac{\partial A_{i+1}}{\partial z} = -\mu_0 I \delta(r - r_0) \tag{23}$$

where

$\mu_0 I \delta(r - r_0)$ – current density

The solution to the system of interface equations obtained in this way was written down as:

$$\begin{matrix}\mathbf{B}_{47} \\ \mathbf{C}_{47}\end{matrix} = \mp\frac{1}{2} e^{\pm\mathbf{q}\, l_1}[(\mathbf{q}\mathbf{u}^{-1}\mathbf{K} \mp \mathbf{V}) e^{\mathbf{u}\, l_1}\mathbf{C}_{57} - (\mathbf{q}\mathbf{u}^{-1}\mathbf{K} \pm \mathbf{V}) e^{-\mathbf{u}\, l_1}\mathbf{B}_{57}] \tag{24}$$

$$\begin{matrix}\mathbf{B}_{57} \\ \mathbf{C}_{57}\end{matrix} = \mp\frac{1}{2} e^{\pm\mathbf{u}\, l_2}[(\mathbf{s}_6^{-1}\mathbf{u}\,\mathbf{K}^{-1} \mp \frac{1}{\mu_6}\mathbf{V}^{-1}) e^{\mathbf{s}_6\, l_2}\mathbf{C}_{67} - (\mathbf{s}_6^{-1}\mathbf{u}\,\mathbf{K}^{-1} \pm \frac{1}{\mu_6}\mathbf{V}^{-1}) e^{-\mathbf{s}_6\, l_2}\mathbf{B}_{67}] \tag{25}$$

$$\begin{matrix}\mathbf{B}_{67} \\ \mathbf{C}_{67}\end{matrix} = \frac{1}{2} e^{\pm\mathbf{s}_6\, l_3} e^{-\mathbf{q}\, l_3}(\mu_6 \pm \mathbf{s}_6\, \mathbf{q}^{-1}) \tag{26}$$

where

$$\mathbf{K} = R_1(\mathbf{v}\, g)\int_0^g J_0(\mathbf{q}r)\, J_0(\mathbf{u}^{\mathbf{T}} r)\, r\, dr + J_1(\mathbf{u}\, g)\int_g^b J_0(\mathbf{q}r)\, R_0(\mathbf{v}^{\mathbf{T}}\, r)\, r\, dr \tag{27}$$

$$\mathbf{V} = R_1(\mathbf{v}\, g)\int_0^g J_1(\mathbf{q}r)\, J_1(\mathbf{u}^{\mathbf{T}} r)\, r\, dr + \frac{1}{\mu_{r5}} J_1(\mathbf{u}\, g)\int_g^b J_1(\mathbf{q}r)\, R_1(\mathbf{v}^{\mathbf{T}}\, r)\, r\, dr \tag{28}$$

The magnetic vector potential for each region of the problem with the coil presented in Fig.2. may be calculated using the equation:

$$A(r, z) = \int_{r_1}^{r_2}\int_{h_1}^{h_2} A_{filamentary}(r, z, r_0, h_0)\, dr_0\, dh_0 \tag{29}$$

After integrating the magnetic vector potential of region 2-3 over the coil's cross section, an expression for the impedance of an I-cored coil placed over the two-layered conductive plate with a surface hole was obtained.

$$Z = \frac{j\omega\pi\mu_0 N^2}{[(r_2 - r_1)(h_2 - h_1)]^2}\chi(\mathbf{m}^{\mathbf{T}} r_1, \mathbf{m}^{\mathbf{T}} r_2)\mathbf{m}^{-4}\{2(h_2 - h_1)\mathbf{m} + e^{\mathbf{m}(h_1 - h_2)} - e^{\mathbf{m}(h_2 - h_1)} - \mathbf{M}\mathbf{N}^{-1}[(\mathbf{T} + \mathbf{U})\, e^{\mathbf{m}\, d}(e^{-\mathbf{m}\, h_1} - e^{-\mathbf{m}\, h_2}) - (\mathbf{T} - \mathbf{U})\, e^{-\mathbf{m}\, d} \times (e^{\mathbf{m}\, h_2} - e^{\mathbf{m}\, h_1})]\}\, \mathbf{m}^{-3}\mathbf{D}^{-1}\chi(\mathbf{m}\, r_1, \mathbf{m}\, r_2) \tag{30}$$

where

$$\chi(\mathbf{m}\, r_1, \mathbf{m}\, r_2) = \int_{\mathbf{m}\, r_1}^{\mathbf{m}\, r_2} r\, L_1'(\mathbf{m}\, r)\, dr \tag{31}$$

$$\mathbf{D} = \int_0^{a_1} J_0(\mathbf{m}\, r) J_0(\mathbf{m}^{\mathbf{T}} r)\, r\, dr + \frac{1}{\mu_f}\int_{a_1}^{a_2} L_0(\mathbf{m}\, r) L_0(\mathbf{m}^{\mathbf{T}} r)\, r\, dr + \int_{a_2}^{b} L_0'(\mathbf{m}\, r) L_0'(\mathbf{m}^{\mathbf{T}} r)\, r\, dr \tag{32}$$

$$\mathbf{T} = \int_0^{a_1} J_0(\mathbf{q}\, r)\, J_0(\mathbf{m}^{\mathbf{T}} r)\, r\, dr + \int_{a_1}^{a_2} J_0(\mathbf{q}\, r)\, L_0(\mathbf{m}^{\mathbf{T}} r)\, r\, dr + \int_{a_2}^{b} J_0(\mathbf{q}\, r)\, L_0'(\mathbf{m}^{\mathbf{T}} r) r\, dr \tag{33}$$

$$\mathbf{U} = \int_0^{a_1} J_1(\mathbf{q}r) J_1(\mathbf{m}^{\mathbf{T}} r)\, r\, dr + \frac{1}{\mu_f} \int_{a_1}^{a_2} J_1(\mathbf{q}r) L_1(\mathbf{m}^{\mathbf{T}} r)\, r\, dr + \int_{a_2}^{b} J_1(\mathbf{q}r) L_1'(\mathbf{m}^{\mathbf{T}} r)\, r\, dr \tag{34}$$

$$\mathbf{M} = (e^{-\mathbf{m}h_1} - e^{\mathbf{m}h_2})[(\mathbf{U}^{-1} + \mathbf{T}^{-1})\,\mathbf{C}_{47} + (\mathbf{U}^{-1} - \mathbf{T}^{-1})\,\mathbf{B}_{47}] - (e^{-\mathbf{m}h_2} - e^{\mathbf{m}h_1})[(\mathbf{U}^{-1} - \mathbf{T}^{-1})\,\mathbf{C}_{47} + (\mathbf{U}^{-1} + \mathbf{T}^{-1})\,\mathbf{B}_{47}] \tag{35}$$

$$\mathbf{N} = (\mathbf{T} + \mathbf{U}) e^{\mathbf{m}d} [(\mathbf{U}^{-1} - \mathbf{T}^{-1})\,\mathbf{C}_{47} + (\mathbf{U}^{-1} + \mathbf{T}^{-1})\,\mathbf{B}_{47}] - (\mathbf{T} - \mathbf{U}) e^{-\mathbf{m}d} [(\mathbf{U}^{-1} + \mathbf{T}^{-1})\,\mathbf{C}_{47} + (\mathbf{U}^{-1} - \mathbf{T}^{-1})\,\mathbf{B}_{47}] \tag{36}$$

The impedance of the coil $Z_0 = R_0 + jX_0$ located in the space with no conductive material was calculated after substituting $\sigma_5 = \sigma_6 = 0$ in (30). Then, by subtracting the Z_0 value obtained in this way from (30), the change of the coil impedance ΔZ was obtained. It was caused by placing the coil over the conductive material with a hole.

$$\Delta Z = Z - Z_0 \tag{37}$$

For applications related to flaw detection (defectoscopy), the change of impedance calculated in relation to the workpiece with no hole proves to be highly significant. The value $\Delta Z_h = \Delta R_h + j\Delta X_h$ obtained in this manner presents the situation where the impedance of the coil placed over the surface of the workpiece has been changed due to the occurrence of a hole.

$$\Delta Z_h = \left| Z - Z_{\,without\ hole} \right| \tag{38}$$

The impedance of the I-cored coil located over the conductive plate with no hole was calculated by substituting $g = 0$ in (30). In such a case $\mathbf{v} = \mathbf{q}$, $\mathbf{K} = \mathbf{E}$, $\mathbf{V} = \mathbf{E}/\mu_5$ and coefficients $\mathbf{C}_{57}$, $\mathbf{B}_{57}$ were reduced to the following form:

$$\begin{aligned} \mathbf{B}_{57} \\ \mathbf{C}_{57} \end{aligned} = \mp\frac{1}{2} e^{\pm \mathbf{s}_5 l_2} [(\mathbf{s}_5 \mathbf{s}_6^{-1} \mp \frac{\mu_5}{\mu_6} \mathbf{V}^{-1}) e^{\mathbf{s}_6 l_2} \mathbf{C}_{67} - (\mathbf{s}_5 \mathbf{s}_6^{-1} \pm \frac{\mu_5}{\mu_6} \mathbf{V}^{-1}) e^{-\mathbf{s}_6 l_2} \mathbf{B}_{67}] \tag{39}$$

3. Results and discussion

The parameters of the coil and the conductive material used in calculations are presented in Table 1. The inductance L_0 was respectively equal to: 3.39 mH for the I-cored coil and 1.89 mH for the air-cored coil. The coil impedance was calculated from (41) while assuming the number of summation terms $Ns = 50$ and the domain radius $b = 12\ r_2$, which corresponds to the value of 54 mm. For the inversion of matrices as well as calculating additional discrete eigenvalues m_i, inv() and fzero() functions available in Matlab were used. The complex values u_i were computed using the approach based on Cauchy's theorem, which is described in detail in [12]. Pursuant to this method the solution domain was divided into rectangles so that each one of them contained not more than one root. Such an approach made it possible to avoid omission of some u_i values.

Table 1. Parameters of the coil, core, and plate used in calculations.

Inner core radius	a_1	0.5 mm
Outer core radius	a_2	1.5 mm
Length	d	5 mm
Inner coil radius	r_1	1.8 mm
Outer coil radius	r_2	4.5 mm
Offset	h_1	0.1 mm
Parameter	h_2	4 mm
Number of turns	N	700
Liftoff	l_1	0.1 mm
Parameter	l_2	2.1 mm
Parameter	l_3	22.1 mm
Relative permeability	μ_f	2000
Relative permeability	μ_5, μ_6	1
Conductivity	σ_5, σ_6	10 MS m^{-1}
Radius of the domain	b	54 mm
Radius of the hole	g	2.5 mm

The results obtained from Matlab calculations were then verified by means of the finite elements method in COMSOL Multiphysics package. The mesh applied for computations was made up of about 31000 triangular elements and 800 edge elements. The highest density of mesh elements was used around the hole edge and under the coil winding. The calculations for changes ΔZ and ΔZ_h of coil impedance were performed for the range of frequencies from 100 Hz to 100 kHz. All results have been normalized in relation to the reactance X_0 and are presented in Fig.4. and Fig.5. The values for changes of the coil impedance components calculated with use of the proposed mathematical model were only different from the results obtained with COMSOL Multiphysics. In the case of resistance changes, such a difference did not exceed 1.21 %, and for changes of reactance, it was not higher than 0.62 %.

Fig.6. presents the coil resistance changes normalized in relation to reactance X_0 after placing the coil over the conductive material with radius varying from $g = 0$ to $g = 10$ mm. Further increase of the radius g led to only insignificant variation of the coil resistance since the highest density of eddy currents occurred in such a part of the conductive material which is located under the winding. The occurrence of the flaw has a far higher influence on resistance than on reactance. For example, when the frequency was $f = 1$ kHz and a surface hole with the radius of $g = 10$ mm was made in the workpiece, the coil reactance changed only by 2 % but its resistance was amended by as much as 184 %.

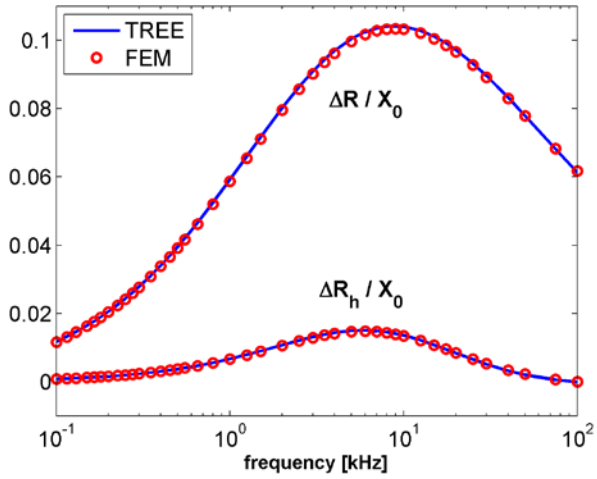

Fig.4. Real part of the normalized impedance changes as a function of frequency.

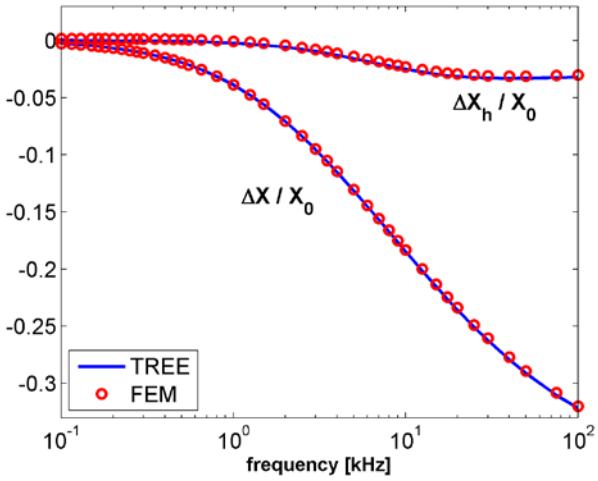

Fig.5. Imaginary part of the normalized impedance changes as a function of frequency.

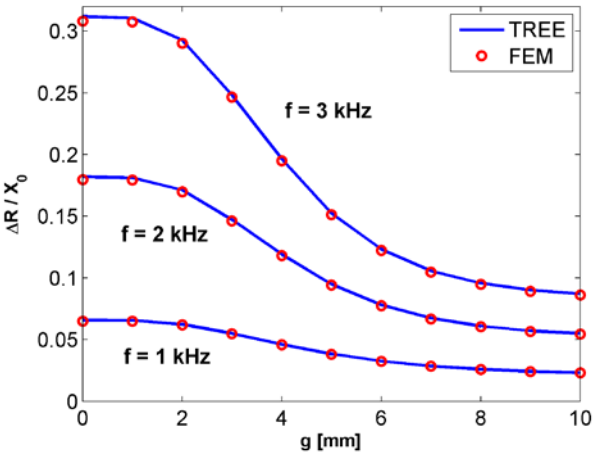

Fig.6. Real part of the normalized impedance changes as a function of the hole radius.

4. CONCLUSION

The axially symmetric mathematical model proposed herein makes it possible to calculate the impedance of an I-cored coil placed over a two-layered conductive plate with a cylindrical surface hole. The final formulas obtained with the use of the TREE method can be implemented in any mathematical software, such as Mathematica or Matlab. Calculations can be made for any size of a hole, even while changing its radius (g) and depth (l_2-l_1). Values of the coil impedance components obtained with the use of proposed solution were verified with the application of the finite elements method. The difference obtained did not exceed 1.21 % for resistance and 0.62 % for reactance within the range of frequency from 100 Hz to 100 kHz. The performed verification of results proved that the mathematical model presented in this work can be used as a substitute for numerical solutions that utilize the finite elements method.

REFERENCES

[1] Theodoulidis, T.P., Bowler, J.R. (2004). The truncated region eigenfunction expansion method for the solution of boundary value problems in eddy current non-destructive evaluation. *Review of Progress in Quantitative Nondestructive Evaluation*, 24A, 403–408.

[2] Kolyshkin, A. (2013). Solution of direct eddy current problems with cylindrical symmetry. In *Proceedings of the International Conference on Application of Contemporary Non-destructive Testing in Engineering*, 4–6 September 2013. Portoroz, Ljubljana, Slovenia: University of Ljubljana, 347–351.

[3] Koliskina, V. (2014). Semi-analytical solution of an eddy current problem for a conducting medium with a surface flaw. *International Journal of Mathematical Models and Methods in Applied Sciences*, 8, 473-480.

[4] Theodoulidis, T.P., Bowler, J.R. (2005). Eddy-current interaction of a long coil with a slot in a conductive plate. *IEEE Transactions on Magnetics*, 41 (4), 1238–1247.

[5] Koliskina, V., Kolyshkin, A. (2015). Mathematical model for eddy current testing of metal plates with two cylindrical flaws. In *IEEE 15th International Conference on Environment and Electrical Engineering (EEEIC)*, 10-13 June 2015, 374-377.

[6] Hao, K., Huang, S., Zhao, W., Wang, S., Dong, J. (2011). Analytical modelling and calculation of pulsed magnetic field and input impedance for EMATs with planar spiral coils. *NDT&E International*, 44 (3), 274–280.

[7] Theodoulidis, T.P., Kriezis, E.E. (2006). *Eddy Current Canonical Problems (With Applications to Nondestructive Evaluation)*. Duluth (Georgia), USA: Tech Science Press.

[8] Lu, Y., Bowler, J.R, Theodoulidis, T.P. (2012). An analytical model of a ferrite-cored inductor used as an eddy current probe. *Journal of Applied Physics*, 111 (10), 103907.

[9] Tytko, G. Dziczkowski, L. (2015). E-cored coil with a circular air gap inside the core column used in eddy current testing. *IEEE Transactions on Magnetics*, 51 (9), 6201804.

[10] Chunfeng, L., Wei, T., Huaming, L., Yingying, J., Hui, Z. (2015). Analytical modeling for the grating eddy current displacement sensors. *Measurement Science Review*, 15 (1), 44-51.

[11] Tytko, G., Dziczkowski, L. (2017). An analytical model of an I-cored coil with a circular air gap. *IEEE Transactions on Magnetics*, 53 (4), 6201104.

[12] Delves, L.M., Lyness, J.N. (1967). A numerical method for locating the zeros of an analytic function. *Mathematics of Computation*, 21 (100), 543–560.

[13] Dellnitz, M., Schütze, O., Zheng, Q. (2002). Locating all the zeros of an analytic function in one complex variable. *Journal of Computational and Applied Mathematics*, 138 (2), 325-333.

Received October 25, 2017.
Accepted February 12, 2018.

MEASUREMENT SCIENCE REVIEW, **18**, (2018), No. 1, 13-19

DE GRUYTER OPEN

MEASUREMENT SCIENCE REVIEW

Journal homepage: http://www.degruyter.com/view/j/msr

ISSN 1335-8871

Research on Measurement Accuracy of Laser Tracking System Based on Spherical Mirror with Rotation Errors of Gimbal Mount Axes

Zhaoyao Shi, Huixu Song, Hongfang Chen, Yanqiang Sun

Beijing Engineering Research Center of Precision Measurement Technology & Instruments, Beijing University of Technology, No.100, Pingleyuan, Chaoyang District, 100124, Beijing, China, shizhaoyao@bjut.edu.cn

This paper presents a novel experimental approach for confirming that spherical mirror of a laser tracking system can reduce the influences of rotation errors of gimbal mount axes on the measurement accuracy. By simplifying the optical system model of laser tracking system based on spherical mirror, we can easily extract the laser ranging measurement error caused by rotation errors of gimbal mount axes with the positions of spherical mirror, biconvex lens, cat's eye reflector, and measuring beam. The motions of polarization beam splitter and biconvex lens along the optical axis and vertical direction of optical axis are driven by error motions of gimbal mount axes. In order to simplify the experimental process, the motion of biconvex lens is substituted by the motion of spherical mirror according to the principle of relative motion. The laser ranging measurement error caused by the rotation errors of gimbal mount axes could be recorded in the readings of laser interferometer. The experimental results showed that the laser ranging measurement error caused by rotation errors was less than 0.1 μm if radial error motion and axial error motion were within ±10 μm. The experimental method simplified the experimental procedure and the spherical mirror could reduce the influences of rotation errors of gimbal mount axes on the measurement accuracy of the laser tracking system.

Keywords: Spherical mirror, laser tracking system, gimbal mount axes, rotation errors, relative motion thinking.

1. INTRODUCTION

Laser tracking system is a large-scale measurement system with high precision in industrial measurement fields, and is similar to a portable coordinate measuring system (PCMS). It is widely applied in shipbuilding, automobile manufacturing, and aircraft manufacturing with requirements of large measuring scale, high measuring efficiency, high measuring precision and simple operation [1]. Rotational motion unit plays an indispensable role in the laser tracking system, and it is also the basic unit for the motions of tracking. However, rotation errors of rotational motion unit may decrease the measurement accuracy of the laser tracking system. Therefore, a special shafting structure can decrease the influences of rotation errors on the outcome of sensors in the laser tracking system and improve the measurement accuracy [2]-[3]. As shown in Fig.1.a), LaserTracer, which holds a stable optical reference sphere as reflection unit, has been developed by English and German national metrology institutes, the NPL and the PTB, and Etalon AG [4]-[7]. Its special shafting structure is named gimbal mount axes (vertical axis and horizontal axis). Laser head, which contains all the optical components as a whole, is driven by gimbal mount axes. As the reflection unit, the reference sphere is mounted on an invar rod that passes through a hollow shaft and is fixed on the bottom of equipment. The position of the reference sphere does not change with the motion of gimbal mount axes. The reference sphere in LaserTracer also possesses a perfect form, with the form error less than 50 nm. In this design, Laser Tracer not only possesses the large measuring angle, but also minimizes the influences of rotation errors on the laser ranging measurement accuracy [8]. As shown in Fig.1.b), in traditional commercial laser trackers, a plan mirror is fixed at the intersection of two axes as the reflection unit inside the instrument to reflect laser beam and the intersection serves as the origin under the spherical coordinate system defined by laser tracker. Laser beam from the instrument points to the origin and is reflected to the measurement space by the mirror [1], [9]. Due to the direct contact with two axes, the position of the mirror is changed by rotation error motions of two axes. The position of laser spot and the angle between laser beam and optical axis are also correspondingly changed, so a traditional commercial laser tracker can hardly avoid the influences of rotation error motions caused by vibration and motility of axes [10]-[11]. The measurement accuracy of the laser tracker is decreased because the measurement error caused by vibration and motility of axes can hardly be compensated [12]-[13].

DOI: 10.1515/msr-2018-0003

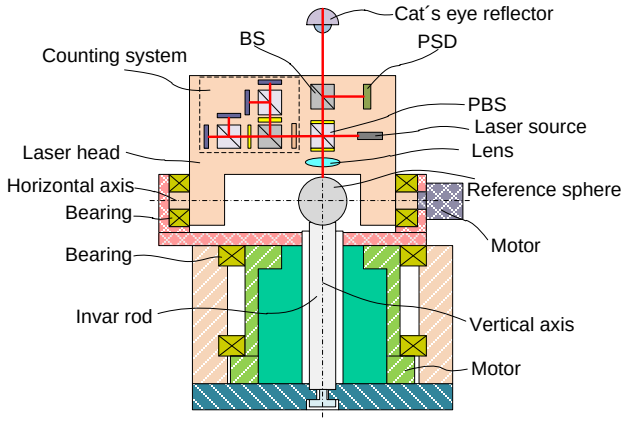

a) Basic structure of LaserTracer.

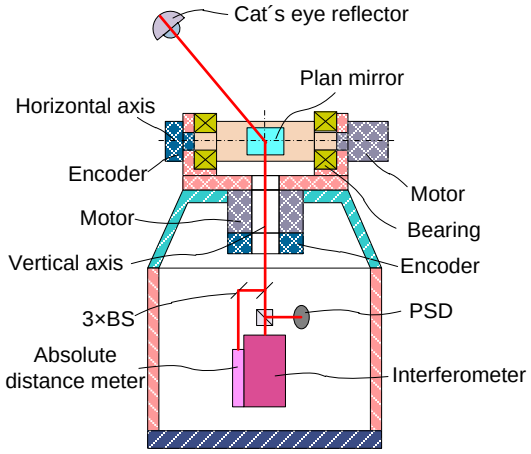

b) Basic structure of Laser Tracker.

Fig.1. Basic structures of two kinds of laser tracking systems.

Up to now, only LaserTracer has used this structure to reduce the influences of rotation errors of gimbal mount axes. However, the characteristic of this structure has not been deeply explored. This paper presents a simplified experimental approach for confirming that the spherical mirror of the laser tracking system can reduce the influences of rotation errors of gimbal mount axes on the measurement accuracy.

2. SUBJECT & METHODS

2.1. Rotation errors in LaserTracer

Interferometer integrated in the laser head of LaserTracer measures the relative displacement from the center of the reference sphere to the center of the cat's eye reflector in 3-D space (Fig.1.a)) [14]. The center of the reference sphere, which is also the intersection point between gimbal mount axes and laser beam, serves as the origin of LaserTracer. The four-way electrical signals emitted by quadrant detector are used to control vertical and horizontal axes so that the laser beam points to the center of the cat's eye reflector and PSD. However, when LaserTracer is tracking the cat's eye reflector, laser spot moves in an irregular direction on the surface of the reference sphere due to the rotation errors (Fig.2.). There are 6 rotation errors for each axis [15]-[16]. The total 12 rotation errors for horizontal axis and vertical axis can be considered as two movements for the laser head because the laser head is connected with gimbal mount axes. The error motions caused by rotation errors can be divided into error motion along the vertical direction of measuring beam and error motion along the direction of measuring beam. The two kinds of error motions should be within the range of ±20 μm.

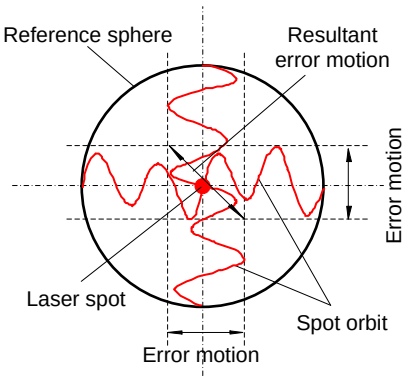

Fig.2. Laser spot orbit on the surface of the reference sphere.

The optical system of LaserTracer is shown in Fig.3. Laser beam from optical fiber passes through the polarization beam splitter (PBS) and is then separated into two parts (polarized beams P and S). Polarized beam P enters the counting system as the reference beam, whereas polarized beam S reflected by PBS, the cat's eye reflector and reference sphere interfere with the reference beam in counting system as measuring beam.

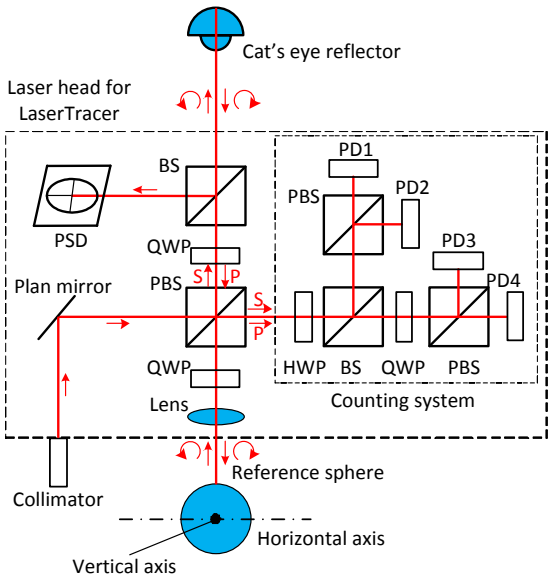

Fig.3. Optical system of LaserTracer.

2.1.1. Error motion along the vertical direction of measuring beam

As shown in Fig.1.a) and Fig.3., rotation error motions of gimbal mount axes in LaserTracer can be transmitted to laser head and all the optical components in laser head. The optical path of the reference beam remains unchanged during the measurement process and the outcome of laser interferometer depends on the variation of the optical path of the measuring beam. The optical path of the measuring beam is determined by the positions of the cat's eye reflector and the reference sphere. Although the positions of cat's eye reflector and reference sphere remain unchanged when the laser head and all optical components are driven by rotation errors of gimbal mount axes, it is not advisable to assume the unchanged optical path of the measuring beam. The focal point of lens deviates from the center of the reference sphere and may cause a certain amount of change of optical path because the lens is also driven by error motions. Therefore, it is necessary to explore the influences of the position variations of lens on measurement error of laser ranging. The complex optical system model of LaserTracer can be simplified because the optical path of the measuring beam in BS and QWPs remains unchanged. Therefore, we can easily explore the relationship between the position variation of optical components (cat's eye reflector, reference sphere, laser head, and measuring beam) and the outcome of laser interferometer.

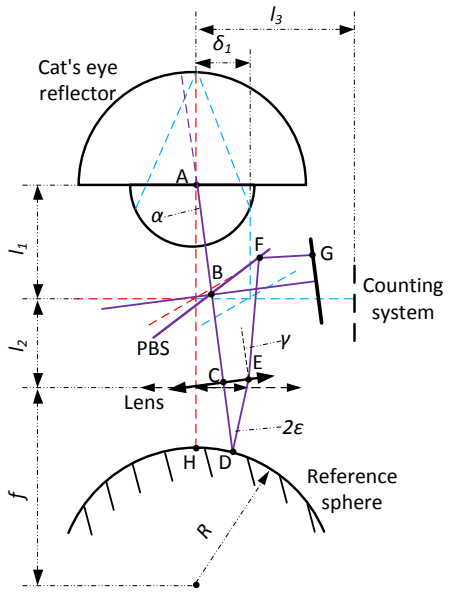

Fig.4. Optical path of measuring beam with error motion along the vertical direction of measuring beam in LaserTracer.

The position variation of measuring beam with the error motion along the vertical direction of measuring beam is shown in Fig.4. l_1 is a variable representing the length between the cat's eye reflector and PBS. l_2=50 mm represents the length between PBS and lens, and l_3=50 mm represents the length between PBS and counting system. Both l_2 and l_3 are constants because all optical components are fixed inside the laser head. f=100 mm represents the focal length and the focal point coincides with the center of reference sphere. R=7.9378 mm represents the radius of reference sphere. δ_1=5 μm represents the offset of measuring beam caused by error motion along the vertical direction of the measuring beam. The values of l_2, l_3, f, and R are given according to the geometry of LaserTracer. It is difficult to precisely measure the geometric parameters of LaserTracer. Therefore, we choose the products of lens and reference sphere from Daheng Optics and HEXAGON. In the measurement process with LaserTracer, the measuring beam moves from red line to blue line. The blue line, which does not point to the center of the cat's eye reflector, will not point to the center of PSD either. Therefore, the signal of PSD controls two motors to ensure that the measuring beam points to the centers of the cat's eye reflector and PSD. Finally, the position of the measuring beam is changed to the purple line. α represents the angle: between the theoretical position (red line without rotation errors) and the actual position (purple line with rotation errors) of the measuring beam. ε represents the incident angle of the measuring beam on the surface of the reference sphere. γ represents the refraction angle of the measuring beam from the lens. Analysis and calculation results indicate the variation of optical path difference between the measuring beam and the reference beam is far less than 1 nm, irrespective of the refractive indices of all the crystals (see (1)). $\Delta_{crystal}$ represents the variation of optical path difference before and after considering the refractive indices under the assumption that $L_{crystal}$=10 cm is the total thickness of all the crystals of LaserTracer. $n_{crystal}$=1.5163 represents the refractive index of K9. γ can be calculated according to (9). Therefore, the influences of refractive indices of all the crystals can be neglected. The actual optical path is $l_{BA}+l_{AD}+l_{DE}+l_{EF}+l_{FG}$. According to the geometric relationship shown in Fig.5. and Fig.6., we can calculate the optical path from the center of the cat's eye reflector to the surface of the reference sphere as well as the optical path from the surface of the reference sphere to the counting system.

$$\Delta_{Crystal} = \left(n_{Crystal} - 1\right) \cdot \frac{\left(1 - \cos\gamma\right)}{\cos\gamma} \cdot L_{Crystal} = 0.17 \text{ nm}. \quad (1)$$

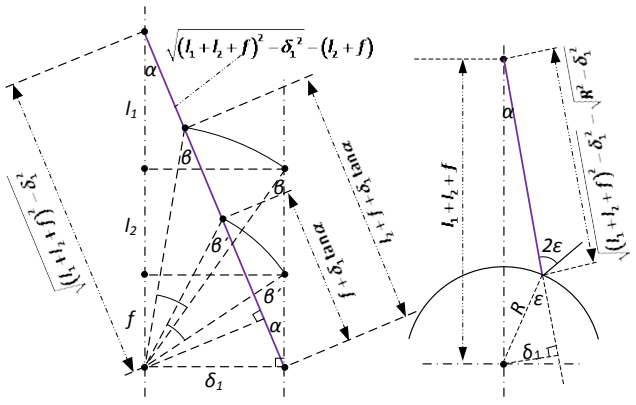

Fig.5. Measuring beam from the cat's eye reflector to the reference sphere.

The optical paths l_{BA} and l_{AD} are respectively given as (2) and (3):

$$l_{BA}=\sqrt{\left(l_1+l_2+f\right)^2-\delta_1^{\,2}}-\left(l_2+f\right); \tag{2}$$

$$l_{AD}=\sqrt{\left(l_1+l_2+f\right)^2-\delta_1^{\,2}}-\sqrt{R^2-\delta_1^{\,2}}\,. \tag{3}$$

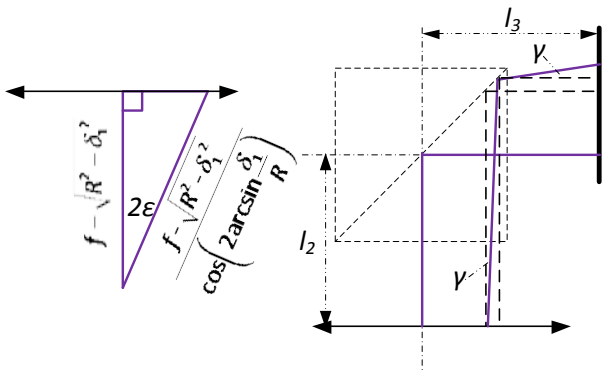

Fig.6. Measuring beam from the reference sphere to the counting system.

The angle between l_{CD} and l_{DE} is given as (4). The optical path l_{DE} is given as (5).

$$2\varepsilon=2\arcsin\frac{\delta_1}{R}; \tag{4}$$

$$l_{DE}=\frac{f-\sqrt{R^2-\delta_1^{\,2}}}{\cos\left(2\varepsilon\right)}\,. \tag{5}$$

The parameters of biconvex lens are provided as follows. R_1=R_2=102.501 mm represents the radii of biconvex lens; t=5 mm represents the thickness of biconvex lens; n=1.5163 represents the refractive index of biconvex lens. d_{in} and θ_{in} represent the pose of beam l_{DE} and is given as (6) and (7):

$$d_{in}=\left(f-\sqrt{R^2-\delta_1^{\,2}}\right)\cdot\tan\left(2\varepsilon\right); \tag{6}$$

$$\theta_{in}=2\varepsilon\,. \tag{7}$$

According to ABCD matrix (8) and the pose of beam l_{DE}, γ is calculated as (9):

$$\begin{bmatrix}d_{out}\\ \theta_{out}\end{bmatrix}=\begin{bmatrix}1 & 0\\ \frac{1-n}{R_1} & n\end{bmatrix}\cdot\begin{bmatrix}1 & t\\ 0 & 1\end{bmatrix}\cdot\begin{bmatrix}1 & 0\\ \frac{1-n}{nR_2} & \frac{1}{n}\end{bmatrix}\cdot\begin{bmatrix}d_{in}\\ \theta_{in}\end{bmatrix}; \tag{8}$$

$$\gamma=\theta_{out}\,. \tag{9}$$

The optical path $l_{EF}+l_{FG}$ is given as (10):

$$l_{EF}+l_{FG}=\frac{l_2+l_3}{\cos\gamma}\,. \tag{10}$$

The optical path difference of measuring beam without error motion along the vertical direction of measuring beam is given as (11):

$$\Delta_1=2\left(l_1+l_2+f-R\right). \tag{11}$$

The optical path difference of measuring beam with error motion along the vertical direction of measuring beam is given as (12):

$$\begin{aligned}\Delta_2=&2\sqrt{\left(l_1+l_2+f\right)^2-\delta_1^{\,2}}-\sqrt{R^2-\delta_1^{\,2}}-\left(l_2+f\right)\\&+\frac{f-\sqrt{R^2-\delta_1^{\,2}}}{\cos 2\varepsilon}+\frac{l_2+l_3}{\cos\gamma}-l_3\end{aligned}\,. \tag{12}$$

We can easily calculate the variation of optical path difference caused by error motion along the vertical direction of measuring beam, as in (13). According to (14), laser ranging measurement error is independent of the displacement between the center of the cat's eye reflector and PBS. According to (15), laser ranging measurement error is less than 0.04 μm when error motion along the vertical direction of measuring beam is around ±5 μm:

$$\begin{aligned}\Delta_{12}=\Delta_2-\Delta_1=&2\sqrt{l_1^{\,2}+300l_1+22499.999975}\\&-2l_1-299.999923\end{aligned}; \tag{13}$$

$$\frac{d\Delta_{12}}{dl_1}=-2+\frac{2\left(150+l_1\right)}{\sqrt{-0.000025+\left(150+l_1\right)^2}}=0; \tag{14}$$

$$\begin{cases}MaxValue[\Delta_{12}]=78\,\text{nm}\\ MinValue[\Delta_{12}]=77\,\text{nm}\end{cases}. \tag{15}$$

2.1.2. Error motion along measuring beam

The position variation of the measuring beam with error motion along the direction of the measuring beam is shown in Fig.7. δ_2=5 μm represents the offset of the measuring beam caused by error motion along the direction of the measuring beam. In the measurement process with LaserTracer, the position of measuring beam does not change. Only the focal point is changed by δ_2 along the direction of the measuring beam, thus changing the diameter of the reflected beam. On the contrary, the optical path difference of measuring beam remains unchanged with error motion along the direction of the measuring beam. Therefore, the laser ranging measurement accuracy is not affected by error motion along the direction of the measuring beam.

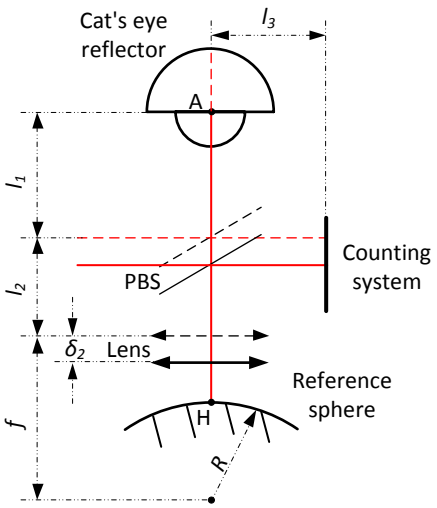

Fig.7. Optical path of measuring beam with error motion along the direction of measuring beam in LaserTracer.

2.2. Our simple model for LaserTracer

The positions of the cat's eye reflector and the reference sphere are fixed, whereas the positions of the measuring beam, PBS and lens are changed, as shown in Fig.4. However, it seems that all components except the reference sphere are fixed. In order to facilitate the experiment process for studying the influences of two types of error motions on the measurement accuracy of laser ranging, it is necessary to simplify the optical system model of LaserTracer. Based on the principle of relative motion, we design a simple optical system model (Fig.8.). Our model has three main advantages.

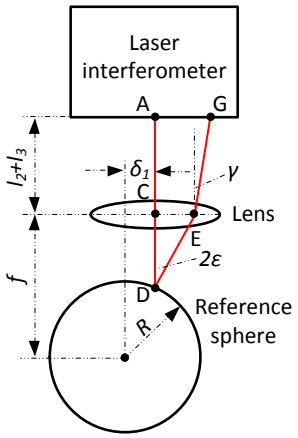

Fig.8. Simple optical system model for LaserTracer.

Firstly, it can use two movements to simulate 12 error motions in gimbal mount axes. Therefore, it is not necessary to build gimbal mount axes and the experimental cost and difficulty are reduced. Secondly, our model does not simulate rotatory movement and new rotation errors are not introduced. In the measurement process with LaserTracer, laser head needs a rotatory movement to make the laser beam point to the center of the cat's eye reflector and PSD. The position of the measuring beam is changed from the red line to the purple line (see Fig.4.). In our model, all the error motions are realized by driving the reference sphere according to the principle of relative motion. Thirdly, fewer uncertainties are introduced into the model because few instruments are used. In order to replace the optical system model of LaserTracer correctly, the parameters in Fig.8. should be consistent with the parameters shown in Fig.4.

2.3. Experimental verification

In the verification experiments, error motions were simulated by driving the reference sphere with the precision positioning platform. Laser interferometer was fixed on a 3D slide table and finely adjusted to ensure laser beam parallels with the plan of optical platform (Fig.9.). A diaphragm was fixed between laser interferometer and biconvex lens. By adjusting the position of biconvex lens, the optical axis overlapped the laser beam. Diaphragm and biconvex lens were fixed near laser interferometer to diminish the dead path error. The precision positioning platform was firstly placed in the vicinity of the focal point of biconvex lens and the reference sphere was then fixed on the precision positioning platform. The position of reference sphere was finely adjusted to ensure that the reflected beam passed through the diaphragm and was irradiated in laser interferometer. Precision positioning platform moved along the red line, and the position of the reference sphere was regarded as the zero position when the outcome of laser interferometer was the lowest. At the same time, the center of reference sphere also overlapped the focal point of biconvex lens. The technical details of PI precision positioning platform are shown in Table 1.

Table 1. Details of PI precision positioning platform.

Model: P-561.3CD		**Units**
Travel	150 × 150 × 150	am
Resolution	0.2	nm
Positioning error	0.03	%
Repeatability	2	nm

The displacement between laser interferometer and lens is 100 mm, which equals the sum of l_2 and l_3. During the experiment, external adjusting devices were removed and not displayed in Fig.9.

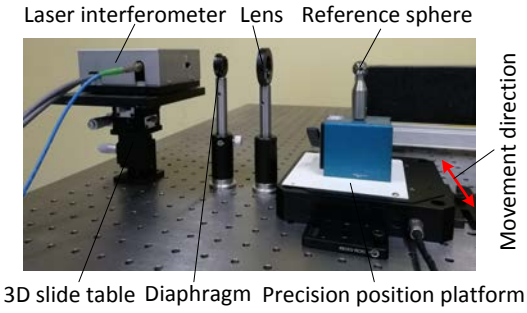

Fig.9. Experimental system for driving reference sphere along the vertical direction of laser beam.

3. RESULTS

Precision positioning platform moved 10 μm, respectively, along the positive and negative directions with the step of 1 μm and 4 groups of data of laser interferometer were recorded. The data of laser interferometer are shown in Table 2. The measurement data curves are shown in Fig.10. The mean curve represents the average value of 4 groups of data. Error bars represent the standard uncertainty (k=2).

Table 2. Data of laser interferometer.

Error motion[μm]	**Outcome of laser interferometer[μm]**				**Standard uncertainty [μm]**
	1st	2nd	3rd	4th	
0	0	0.01	0.02	0.01	0.01
1	0.03	0.01	0.03	0.02	0.01
2	0.03	0.03	0.02	0.04	0.01
3	0.04	0.04	0.03	0.05	0.01
4	0.04	0.03	0.05	0.05	0.01
5	0.05	0.04	0.05	0.05	0.01
6	0.07	0.06	0.06	0.07	0.01
7	0.06	0.07	0.07	0.05	0.01
8	0.05	0.06	0.06	0.07	0.01
9	0.07	0.07	0.06	0.06	0.01
10	0.07	0.08	0.07	0.04	0.02
0	0	-0.01	0	-0.01	0.01
-1	0.01	0	0.02	0.01	0.01
-2	0.02	0.01	0.03	0.02	0.01
-3	0.02	0.01	0.04	0.03	0.01
-4	0.04	0.02	0.03	0.02	0.01
-5	0.04	0.04	0.04	0.03	0.01
-6	0.05	0.05	0.04	0.03	0.01
-7	0.06	0.04	0.04	0.05	0.01
-8	0.05	0.02	0.06	0.04	0.02
-9	0.06	0.04	0.04	0.05	0.01
-10	0.07	0.05	0.05	0.04	0.01

The standard deviation of results is calculated in (16) and shown in Table 2. Standard uncertainty caused by repeatability of measurement is given as (17) where (k=2). n' represents the measurement times at the same error motion. l_i represents the i_{th} data of laser interferometer.

$$\sigma=\sqrt{\frac{\sum_{i=1}^{n'}\left(l_i-\bar{l}\right)}{n'-1}}; \tag{16}$$

$$u=k\cdot\frac{\sigma}{\sqrt{n'}}. \tag{17}$$

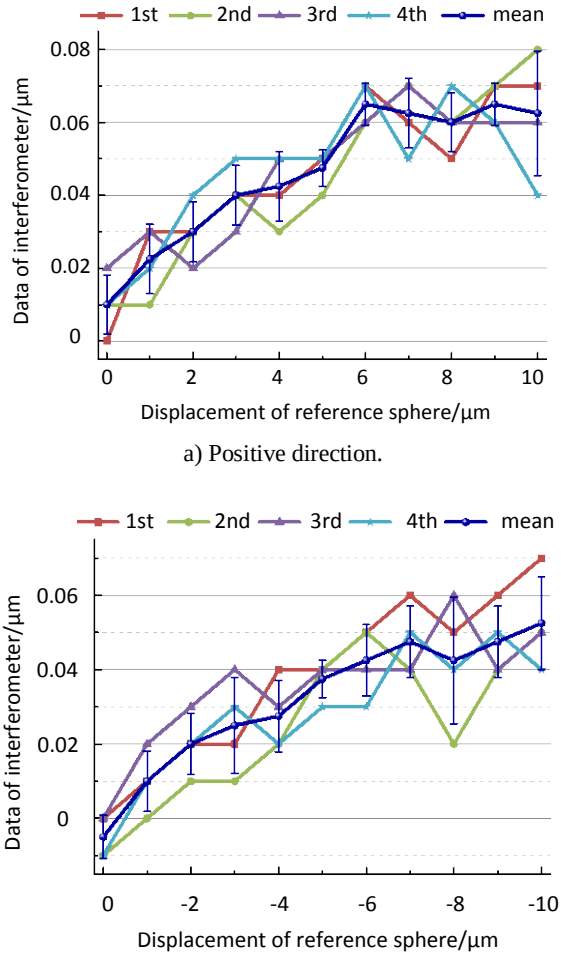

a) Positive direction.

b) Negative direction.

Fig.10. Experimental results of driving reference sphere along the vertical direction of laser beam.

When error motion along the positive direction is less than 5 μm, the maximum laser ranging measurement error is 0.05 μm; when error motion along the negative direction is less than -5 μm, the maximum laser ranging measurement error is 0.04 μm. According to the above theoretical analysis, when error motion is ±5 μm, the maximum laser ranging measurement error is 0.04 μm, which is consistent with the experimental result. The laser ranging measurement error still climbs to 0.08 μm when error motion increases to 10 μm. Both measuring result and error trend are consistent with the theoretical analysis, indicating that our simple model can replace the complex model of LaserTracer correctly. Moreover, theoretical and experimental data have verified that the spherical mirror of the laser tracking system can decrease the influences of rotation errors of gimbal mount axes.

4. DISCUSSION & CONCLUSIONS

In Fig.10., the data measured along the positive direction are slightly larger than those measured along the negative direction. The reason is that zero positions for positive and negative directions do not overlap well with each other.

According to theoretical and experimental result, error motion should be controlled within ±20 μm. When error motion is more than ±20 μm, the reflected beam is away from the cat's eye reflector or PSD, thus resulting in the separation of measuring beam and reference beam.

There are two reasons causing the little difference between theory and experiment in laser ranging measurement error. In Fig.4., error motion is a composite motion involving the main horizontal component and a tiny vertical component. PI precision positioning platform might be not extremely accurate. In the field of ultra-precision measurement, any tiny variation in the system might lead to inaccurate measurement results.

The analysis method and experiment scheme in this paper confirm that the spherical mirror of the laser tracking system can decrease the influences of rotation errors of gimbal mount axes on the measurement accuracy. Laser ranging measurement error caused by rotation errors is less than 0.1 μm if rotation error motions are within ±10 μm. The results might be utilized to reduce the cost and the design requirements of the laser tracking system. Furthermore, studying the structure, which can decrease the influences of rotation errors in the readings of sensors, would be conducive to develop the research for form errors of cylindrical parts.

ACKNOWLEDGMENT

The work was supported by Beijing Municipal Science and Technology Commission [Z161100001516003], and National Key Scientific Instrument and Equipment Development Project of China [No.2013YQ17053904].

REFERENCES

[1] Harding, H. (2013). *Handbook of Optical Dimensional Metrology*. CRC Press, Vol. 3, 95-104.

[2] Schneider, C.T. (2004). LaserTracer – A new type of self tracking laser interferometer. In *8th International Workshop on Accelerator Alignment*, 4-7 October 2004. Geneva, Switzerland : European Laboratory for Particle Physics, 1-6.

[3] Peggs, G.N., Maropoulos, P.G., Hughes, E.B., Forbes, A.B., Robson, S., Ziebart, M., Muralikrishnan, B. (2009). Recent developments in large-scale dimensional metrology. *Proceedings of the Institution of Mechanical Engineers, Part B: Journal of Engineering Manufacture*, 223 (6), 571-595.

[4] Schwenke, H., Schmitt, R., Jatzkowski, P., Warmann, C. (2009). On-the-fly calibration of linear and rotary axes of machine tools and CMMs using a tracking interferometer. *CIRP Annals - Manufacturing Technology*, 58, 477-480.

[5] Schwenke, H., Franke, M., Hannaford, J., Kunzmann, H. (2005). Error mapping of CMMs and machine tools by a single tracking interferometer. *CIRP Annals - Manufacturing Technology*, 54, 475-478.

[6] Camboulives, M., Lartigue, C., Bourdet, P., Salgado, J. (2016). Calibration of a 3D working space by multilateration. *Precision Engineering*, 44, 163-170.

[7] Gąska, A., Sładek, J., Ostrowska, K., Kupiec, R., Krawczyk, M., Harmatys, W., Gąska, P., Gruza, M., Owczarek, D., Knapik, R., Kmita, A. (2015). Analysis of changes in coordinate measuring machines accuracy made by different nodes density in geometrical errors correction matrix. *Measurement*, 68, 155-163.

[8] Muralikrishnan, B., Lee, V., Blackburn, C., Sawyer, D., Phillips, S., Ren, W., Hughes, B. (2013). Assessing ranging errors as a function of azimuth in laser trackers and tracers. *Measurement Science and Technology*, 24, 065201.

[9] Muralikrishnan, B., Phillips, S., Sawyer, D. (2016). Laser trackers for large-scale dimensional metrology: A review. *Precision Engineering*, 44, 13-28.

[10] Hughes, B., Forbes, A., Lewis, A., Sun, W.J., Veal, D., Nasr, K. (2011). Laser tracker error determination using a network measurement. *Measurement Science and Technology*, 22, 045103.

[11] Feng, D.Y., Gao, Y.G., Zhang, W.B. (2011). Elimination of shafting errors in photoelectrical theodolites with standard-bearings. *Optics and Precision Engineering*, 19, 605-611.

[12] Conte, J., Majarena, A.C., Acero, R., Santolaria, J., Aguilar, J.J. (2015). Performance evaluation of laser tracker kinematic models and parameter identification. *The International Journal of Advanced Manufacturing Technology*, 77, 1353-1364.

[13] Acero, R., Santolaria, J., Pueo, M., Brau, A. (2016). Real-time laser tracker compensation of a 3-axis positioning system-dynamic accuracy characterization. *The International Journal of Advanced Manufacturing Technology*, 84, 595-606.

[14] Lee, H.W., Chen, J.R., Pan, S.P., Liou, H.C., Hsu, P.E. (2016). Relationship between ISO 230-2/-6 test results and positioning accuracy of machine tools using LaserTRACER. *Applied Sciences*, 6, 105.

[15] International Organization for Standardization. (2006). *Test code for machine tools - Part 7: Geometric accuracy of axes of rotation*. ISO 230-7:2006.

[16] Zhao, J.T., Hu, X.D., Zou, J., Zhao, G.Y., Lv, H.Y., Xu, L.Y., Xu, Y., Hu, X.T. (2016). Method for correction of rotation errors in Micro-CT System. *Nuclear Instruments and Methods in Physics Research A*, 816, 149-159.

Received September 11, 2017.
Accepted January 29, 2018.

MEASUREMENT SCIENCE REVIEW, **18**, (2018), No. 1, 20-27

DE GRUYTER OPEN

MEASUREMENT SCIENCE REVIEW

Journal homepage: http://www.degruyter.com/view/j/msr

ISSN 1335-8871

Measurement System Analyses – Gauge Repeatability and Reproducibility Methods

Lenka Cepova[1], Andrea Kovacikova[1], Robert Cep[1], Pavel Klaput[2], Ondrej Mizera[1]

[1]Department of Machining, Assembly and Engineering Metrology, Faculty of Mechanical Engineering, VSB-Technical University of Ostrava, 17. listopadu 15/2172, 708 33 Ostrava, Czech Republic, lenka.cepova@vsb.cz.
[2]Department of Quality Management, Faculty of Metallurgy and Material Engineering, VSB-Technical University of Ostrava, 17. listopadu 15/2172, 708 33 Ostrava, Czech Republic.

The submitted article focuses on a detailed explanation of the average and range method (Automotive Industry Action Group, Measurement System Analysis approach) and of the honest Gauge Repeatability and Reproducibility method (Evaluating the Measurement Process approach). The measured data (thickness of plastic parts) were evaluated by both methods and their results were compared on the basis of numerical evaluation. Both methods were additionally compared and their advantages and disadvantages were discussed. One difference between both methods is the calculation of variation components. The AIAG method calculates the variation components based on standard deviation (then a sum of variation components does not give 100 %) and the honest GRR study calculates the variation components based on variance, where the sum of all variation components (part to part variation, EV & AV) gives the total variation of 100 %. Acceptance of both methods among the professional society, future use, and acceptance by manufacturing industry were also discussed. Nowadays, the AIAG is the leading method in the industry.

Keywords: GRR study approach, the average and range method, the honest GRR study.

1. INTRODUCTION

As R. Hart and M. Hart [1] claim, in a manufacturing process the perceived variation includes both the true, but unknown product variation (part to part variation) and the measurement system variation. When the perceived variation of a manufacturing process is too large, a measurement system study is needed to determine whether the improvement efforts should be made in the measurement process. The correct production process and part evaluation is conducted based on appropriately measured data and it is a technical necessity. Knowles a Vickers [2] highlight that the measured data are the core stones for the decision making process and these decisions are made under fully reliable circumstances. Therefore, in the serial production exist many standards, as e.g., IATF 16 949 (automotive industry) [3], regulations and quality tools, e.g., ISO, QS – 9000 [4] that govern this problematic. Especially the requirements on serial production in the automotive industry are very strict. An important role plays quality planning by product development according to a set of techniques called APQP (Advanced product quality planning) [5]. The points of APQP manual - subhead 4.2 - recommend for all processes in control plan their verification in accordance to measurement system analyses for specified measuring and monitoring gages. Hermans a Liu [6] claim that the measurement system analysis together with process failure mode and effect analysis (PFMEA) and control plan belong to the most important steps by new product development (NPD). The measurement system analysis is mainly conducted in accordance with:

- methods offered by the reference guideline of Chrysler, Ford and General Motors Company, called measurement system analyses (AIAG, MSA) [7],
- methods for evaluating the measurement process (EMP approach, Dr. Wheeler) [8],
- VDA5 methods – Measurement Process Qualification [9].

The detailed comparison of MSA and VDA5 approach is available, e.g., in thesis [10]. The overview of variability characteristic, such as stability, bias, linearity, repeatability and reproducibility are available for example in the publication of Dietrich and Schulze [11] or in the article of Kazerouni [12]. In the submitted article the attention is paid to the methods of measurement system variability analyses. The chosen methods are the range and average method (MSA, AIAG) [7] and the honest GRR study (EMP approach, Wheeler) [8].

Increase of the quality of manufactured products caused increase in the amount of research about techniques [30] used successfully to reduce the manufacturing defects [31].

DOI: 10.1515/msr-2018-0004

2. MEASUREMENT TASK DEFINITION

The chosen measured part for the experiment purpose was the front cover of compact wheel loader (Fig.1.). The specified part is manufactured by thermoforming technology [13] on the machine GEISS. The raw material is from PMMA boards with thickness of 8 mm. According to the drawing documentation the specified material thickness after thermoforming should be 4 mm with tolerance -1.5/+1.5 mm. This request meets the defined surface tolerance. Beyond the surface tolerance the minimal part thickness of 3.5 mm is defined.

Parts for the measurement activities were collected gradually out of the manufacturing process. As the authors of Rolls–Royce guideline [14] highlight by conducting the measurement system analyses, it is important that chosen parts cover the full manufacturing tolerances. Therefore, one part from each production shift was collected in order to have ten parts available with full production tolerance coverage (GRR study requirement). Consequently, the parts were numbered on their inner surface from 1 to 10. The measurement activities were conducted in the metrological laboratory with calibrated measurement devices (thickness gage) and three operators, who regularly conducted measurements of this specified part. As step one the first operator has measured all parts, then the second operator and at last the third operator.

All measurements were conducted with respect to the statistical measurement independence by hiding the measured part number. It means that operators did not know which part number they were measuring. The measured values were not written into the gage repeatability and reproducibility data collection sheet for measurement system analyses, but they were noted down in an Excel spreadsheet. The measured data overview is available in Table 1.

Table 1. Data of measurement II - plastic part [mm].

Operator 1					
Meas.	1	2	3	4	5
1. trial	5.03	4.82	4.93	5.01	5.14
2. trial	5.02	4.94	4.81	5.03	5.03
3.trial	5.01	4.84	4.93	5.00	5.02
Meas.	6	7	8	9	10
1. trial	5.23	4.89	5.13	4.93	4.97
2. trial	5.21	4.87	5.02	4.91	4.98
3.trial	5.23	4.92	5.03	5.01	4.95
Operator 2					
Meas.	1	2	3	4	5
1. trial	5.13	4.78	4.83	4.99	5.03
2. trial	5.03	4.79	4.82	4.99	5.03
3.trial	5.03	4.78	4.94	4.98	5.03
Meas.	6	7	8	9	10
1. trial	5.22	4.88	5.00	5.02	5.00
2. trial	5.11	4.89	5.00	4.94	5.03
3.trial	5.22	4.78	4.98	4.92	5.02
Operator 3					
Meas.	1	2	3	4	5
1. trial	5.03	4.77	4.82	5.02	4.99
2. trial	5.04	4.78	4.82	5.14	5.03
3.trial	5.13	4.89	4.80	5.01	5.1
Meas.	6	7	8	9	10
1. trial	5.22	4.92	5.02	4.94	5.03
2. trial	5.22	4.94	5.14	4.92	5.01
3.trial	5.24	4.94	5.02	4.91	5.14

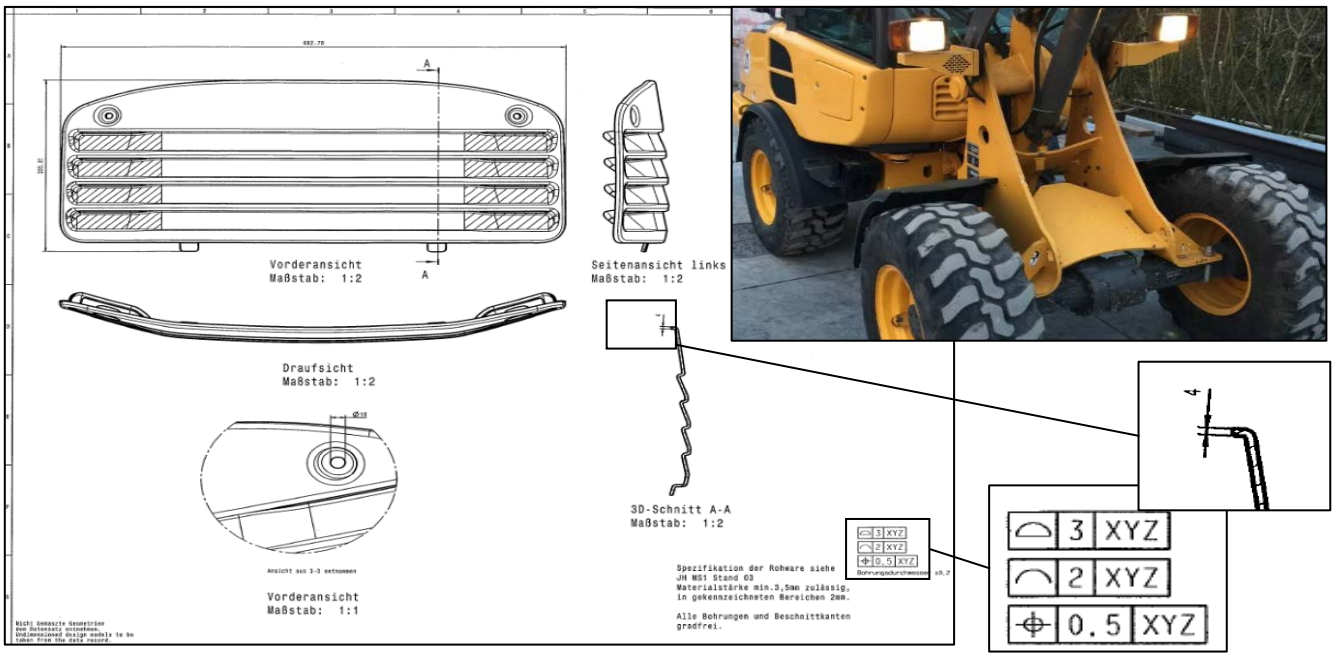

Fig.1. Drawing cut out – a plastic part of compact wheel loader cabin front area.

3. AVERAGE AND RANGE METHOD

The average and range method ($\overline{X}$, $\overline{R}$) is a method for measurement system evaluation of continues scale. The results of this method have to be interpreted based on graphical and numerical results as it is highlighted by Klaput [9]. The advantage of this method is in its possibility to fracture the variability components to:

- Measurement gage variability (repeatability),
- Operator variability (reproducibility).

The disadvantage of this method is that it does not take into consideration the operator and part or measurement gage interactions. The mentioned statement is also confirmed in the submitted article of Healy and Wallce [15]. The method progress consists of few logically followed steps. At the beginning is evaluated the statistical process stability from repeatability point of view by repeated measurements based on average chart and range chart. The detailed examination of both graphs belongs to the graphical outputs of the average and range method, which are available, e.g., in the statistical software Minitab [16]. After the statistical process stability is confirmed, the measurement system evaluation is continued by numerical step by step evaluation.

At first, the measurement repeatability EV is estimated according to (1).

$$EV = \hat{\sigma}_{pe} = \frac{\bar{\bar{R}}}{d_2} \tag{1}$$

where,

$\bar{\bar{R}}$ – the average variation range of all operators' repeated measurements for all parts,

d_2 – correction factor for values link to the distribution of average variation (see appendix C in MSA, AIAG guideline) [7]. It is necessary to look for this coefficient in the penultimate line, whereas m = number of repeated measurement trials. For m = 3 –> $d_2 = 1.69257$.

In the next step, the measurement reproducibility AV is calculated according to (2).

$$AV = \hat{\sigma}_o = \sqrt{\left(\frac{\bar{R}_{DIFF}}{d_2}\right)^2 - \frac{o}{o.n.r} * EV^2} \tag{2}$$

where

$\bar{R}_{DIFF}$ – is the variation range of repeated measurement for each measured part by single operator calculated according to (3).

r – number of measured parts,

n – number of repeated measurement trials,

o – number of operators,

d_2 – correction factor for values link to the distribution of average variation (see appendix C in MSA, AIAG guideline) [7]. It is necessary to look for this coefficient as g (number of subgroups) = 1 (fixed factor) and m (subgroup range) = number of operators (variable). For m = 3 (conducted measurement task) –> $d_2 = 1.91155$.

$$\bar{R}_{DIFF} = |\bar{R}_{MAX} - \bar{R}_{MIN}| \tag{3}$$

where,

$\bar{R}_{MAX}$ – largest arithmetical average for one of the three operators,

$\bar{R}_{MIN}$ – smallest arithmetical average for one of the three operators

In the following steps, there is the possibility to process with evaluation of combined gage the repeatability and reproducibility GRR according to (4).

$$\text{GRR} = \hat{\sigma}_e = \sqrt{EV^2 + AV^2} \tag{4}$$

The calculated GRR value does not have any ability. The measurement system suitability (% GRR – percentage of repeatability and reproducibility) is possible to evaluate just after the comparison of repeatability and reproducibility (measurement system variability) with the total variability TV (process variability), that is calculated by (5).

$$TV = \hat{\sigma}_x = \sqrt{GRR^2 + PV^2} \tag{5}$$

where,

PV – part variability calculated according to (6):

$$PV = \hat{\sigma}_p = \frac{R_p}{d_2} \tag{6}$$

where,

Rp – the variation range from the measurement of arithmetic mean of the individual repeats for the individual subgroups of the parts.

d_2 – correction factor for values link to the distribution of average variation (see appendix C in MSA, AIAG guideline) [7]. It is necessary to look for this coefficient as g (number of subgroups) = 1 (fixed factor) and m (subgroup range) = number of measured parts (variable). For m = 10 (No. of measured parts) –> $d_2 = 3.17905$.

The penultimate step after the TV value calculation is the calculation of measurement system suitability indicator % GRR – gage repeatability, % AV – reproducibility, and % PV – product variability. The % GRR – value of repeatability and reproducibility is calculated according to (7), what is the proportion of combined repeatability and reproducibility divided by total variability and multiplied by 100. The value called % GRR is interpreted as the percentage of total variation that redounds to the combined repeatability (EV) and reproducibility (AV)

$$\%\,GRR = 100 . \frac{GRR}{TV} \tag{7}$$

The percentage representation of repeatability % EV is calculated according to (8), where the parameter called % EV refers to the percentage value of total variability that redounds to the equipment variability.

$$\%\,EV = 100 . \frac{EV}{TV} \tag{8}$$

The percentage representation of the second variability component – reproducibility % AV is calculated according to (9), where the parameter called % AV refers to the percentage value of total variability that redounds to the operator variability.

$$\%AV = 100 . \frac{AV}{TV} \quad (9)$$

As the second to the last one the percentage representation of product variability % PV is calculated according to (10). The parameter called % PV refers to the percentage value of total variability that redounds to the part to part variability.

$$\%PV = 100 . \frac{PV}{TV} \quad (10)$$

As the last step in this method the ndc parameter (number of district categories) is calculated, where by this calculation is defined the number of district categories that can be distinguished by the measurement system. AIAG [7] and also Minitab guideline [16] calculates the ndc parameter according to (11).

$$ndc = 1.41 . \frac{PV}{GRR} \quad (11)$$

The outcome for average and range method is about making a decision whether the measurement system is acceptable, conditionally acceptable or not acceptable based on the decision making matrix for measurement system evaluation based on two criteria (AIAG approach [7]). The first criterion is % GRR, see Table 2., and the second criterion is ndc parameter, see Table 3. On the border values (% GRR, ndc) are also different angles of view as stated by Dietrich and Schulze [11].

Table 2. The border values of % GRR [7].

$\%GRR < 10\%$	Acceptable measurement system. The measurement system provides reliable information about the process changes.
$10\% < \%GRR < 30\%$	Conditionally acceptable measurement system. It can be used for some applications.
$\%GRR > 30\%$	Not acceptable measurement system. The measurement system does not provide reliable information about the process changes.

Table 3. The border values of ndc [7].

$ndc \geq 5$	Acceptable measurement system. The measurement system provides reliable information about the process changes.
$ndc < 5$	Not acceptable measurement system. The measurement system does not provide reliable information about the process changes.

4. THE HONEST GRR STUDY (EMP)

The honest GRR study belongs to the EMP methods [8] - Evaluating the measurement process, what are the methods for measurement system evaluation. As G. Knowlers [17] highlights a variability reduction, it belongs today to the interest of the manufacturing companies. The EMP method bases were developed in the 80's by the American statistician and awarded quality expert Dr. Wheeler [18]. A part of the EMP methods is also the honest GRR study. The method is nowadays a part of debates among professionals, e.g. [19], [20], there exist qualification courses for its introduction and implementation (mainly in the USA) and EMP macros are available by some statistical software as, e.g. the SAS7QC software [22]. In order to evaluate the consistency, this method uses regulation charts that can detect bias between operators (reproducibility) or inconsistency between operators. For measurement error evaluation the honest GRR study based on the Fisher intraclass correlation coefficient is used. By the value of intraclass correlation coefficient the measurement system is divided into four groups (class monitors): first, second, third, and fourth [8]. Each single monitor class is characterized by its ability to attenuate the production process signals in regular chart, the ability to detect shift and to detect the production process improvement. From this point of view the individual class monitors are characterized according to three factors [22]:

- Attenuation of process signals,
- Chance to detect a shift,
- Measurement system ability to track the process improvement.

Here applies the rule, the higher number of class monitor there is (max. class monitor 4), the greater percentage of variance there is due to measurement system variability. The overall systematic review of four class monitors and their factor characteristics is shown in Table 4.

Table 4. Measurement system class of monitor and their characteristics for different r_0 [23].

Intraclass correlation	Class monitor	Attenuation of Process Signals	Chance of detecting a 3 Std, Error shift n = 10	Ability to track Process Improvements
0.80 – 1.00	First	Less then 10 %	More than 99% with rule one	Up to C_{p80}
0.50 – 0.80	Second	10 % – 30 %	More than 88% with rule one	Up to C_{p50}
0.20 – 0.50	Third	30 % – 55 %	More than 91% with rule 1. – 4.	Up to C_{p20}
0.00 – 0.20	Fourth	More then 55 %	Rapidly Vanishes	Unable to track

The first introduced factor is attenuation of process signals that determine into how many percentages can the measurement system attenuate the production process signal (to degrade the information provided by process variability). It means to attenuate the observed variance in comparison to the real variance. The interaction between the production process signals and the measurement system signals is visible in Fig.2., where on the x-axis the intraclass correlation coefficient (r_0) is shown and on the y-axis is signal strength in percentage.

The second important factor is the chance of detecting a 3-standard error shift according to Western electric rules by the subgroup of ten parts [24]. In accordance to Wachsa [24], it is very important to detect the shift in production process, because when it is not done there is a risk of facing an error of type II, which means that the nonconformity part is evaluated as conformity part. It means that the regular chart has to detect the measurement above the UCL (upper control line) or LCL (lower control line), but it is not the case.

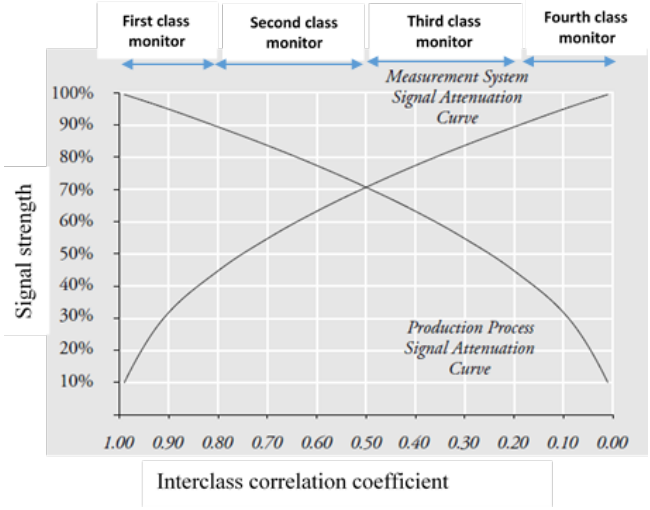

Fig.2. Attenuation of production process and measurement system signals.

The last introduced factor is linked with the chance to detect the process improvement (see the classification borders in Table 2.). The last column of Table 2. shows how big must the process improvement or weakening be for the process to be moved from one class monitor into the other.

The analytical part of the honest GRR consists, similarly to the average and range method, of some systematically following steps. The first step is counting repeatability of variance component according to (12).

$$\left(\hat{\sigma}_{pe}\right)^2 = EV^2 = \left(\frac{\bar{\bar{R}}}{d_2}\right)^2 \tag{12}$$

where,

$\bar{\bar{R}}$ – the average variation range of all operators repeated measurements for all parts,

d_2 – correction factor for values link to the distribution of average variation (see appendix C in MSA, AIAG guideline) [7]. It is necessary to look for this coefficient in the penultimate line, whereas m = number of repeated measurement trials. For m = 3 –> $d_2 = 1.69257$.

The second step is counting the variance component called reproducibility according to (13). $\bar{R}_{DIFF}$ is calculated the same as by the average and range method and it is according to the already mentioned (13).

$$(\hat{\sigma}_o)^2 = AV^2 = \left\{\left[\left(\frac{\bar{R}_{DIFF}}{d_2}\right)\right]^2 - \frac{o}{o.n.r}.\left(\hat{\sigma}_{pe}\right)^2\right\} \tag{13}$$

For (13) apply:

r – number of measured parts,

n – number of repeated measurement trials,

o – number of operators,

d_2 – correction factor for values link to the distribution of average variation (see appendix C in MSA, AIAG guideline) [7]. It is necessary to look for this coefficient as g (number of subgroups) = 1 (fixed factor) and m (subgroup range) = number of operators (variable). For m = 3 (conducted measurement task) –> $d_2 = 1.91155$.

The next step is calculating the combined repeatability and reproducibility according to (14) and the total variation according to (15).

$$(\hat{\sigma}_e)^2 = GRR^2 = \left(\hat{\sigma}_{pe}\right)^2 + (\hat{\sigma}_o)^2 \tag{14}$$

$$(\hat{\sigma}_x)^2 = TV^2 = \left(\hat{\sigma}_p\right)^2 + (\hat{\sigma}_e)^2 \tag{15}$$

Because the second power of the part variance is not known, it is necessary to calculate it according to (16).

$$\left(\hat{\sigma}_p\right)^2 = PV^2 = \left[\frac{R_p}{d_2}\right]^2 \tag{16}$$

where,

Rp – the variation range from the measurement of arithmetic mean of the individual repeats for the individual subgroups of the parts.

d_2 – correction factor for values link to the distribution of average variation (see appendix C in MSA, AIAG guideline) [7]. It is necessary to look for this coefficient as g (number of subgroups) = 1 (fixed factor) and m (subgroup range) = number of measured parts (variable). For m = 10 (No. of measured parts) –> $d_2 = 3.17905$.

The next step is calculating the percentage component of combined repeatability and reproducibility % GRR (17), also the percentage component value of variance component repeatability (18) and reproducibility component (19).

$$\%\,GRR = 100.\frac{(\hat{\sigma}_e)^2}{(\hat{\sigma}_x)^2} \tag{17}$$

$$\%\,GRR = 100.\frac{(\hat{\sigma}_e)^2}{(\hat{\sigma}_x)^2} \tag{18}$$

$$\%\,AV = 100.\frac{(\hat{\sigma}_o)^2}{(\hat{\sigma}_x)^2} \tag{19}$$

The intraclass correlation coefficient is calculated according to (20) and on its basis the measurement system is classified in one of four class monitors.

$$r_0 = \frac{(\hat{\sigma}_p)^2}{(\hat{\sigma}_x)^2} \quad (20)$$

The penultimate step is the process signals attenuation calculation (21).

$$attenuation\ of\ process\ signals = 1 - \sqrt{r_0} \quad (21)$$

The last step is calculating the process improvement detection according to (22), (23), and (24).

$$C_{p80} = \frac{USL-LSL}{6.\left(\frac{\bar{R}}{d_2}\right)} . \sqrt{1-0.80} \quad (22)$$

$$C_{p50} = \frac{USL-LSL}{6.\left(\frac{\bar{R}}{d_2}\right)} . \sqrt{1-0.50} \quad (23)$$

$$C_{p20} = \frac{USL-LSL}{6.\left(\frac{\bar{R}}{d_2}\right)} . \sqrt{1-0.20} \quad (24)$$

5. GRR ANALYSES COMPARISON BASED ON RESULTS GAINED BY TWO METHODS (AVERAGE AND RANGE METHOD AND THE HONEST GRR STUDY)

In this article subhead, the results of GRR analysis (see Table 5.) based on two methods are compared:

- average and range method,
- the honest GRR study.

The average and range method evaluate the measurement system as not acceptable, because the % GRR = 33.41 and is more than 30 % and the ndc parameter has the value 3, which is also not an acceptable value of the ndc parameter. The variability component called repeatability has the value 32.23 %, the reproducibility component is 8.81 %, the part variability component is 94.25 %. It means that by each variability component sum, the total variability is more than 100 %, which is a bit difficult to agree by mathematical rules. Reason for that is the counting variability component as standard deviation by AV & GRR.

According to the honest GRR study the analyzed measurement system is evaluated as first-class monitor, because the intraclass correlation coefficient has reached the value 0.89. Same as by the average and range method, each variability component can be defined separately. The variability component repeatability has a value of 10.38 %, the variability component reproducibility has a value of 0.78 %, the combined variability component repeatability and reproducibility has a value of 11.16 %. The total variability value is obtained by counting all partial components and is 100 %. The process signal attenuation will be 5.74 % and the measurement system attenuation will be 94.26 % (the observed process will be very similar to the real process). For the first class monitor measurement process there will be more than 99 % probability of detecting the 3-standard deviation shift by number of subgroups 10 based on the Western Union rule No. I. The measurement system has the ability to track the process improvement up to C_{p80} where the value is 2.79.

Table 5. Results of GRR analyses for the measured data in Table 1.

Average and range method (AIAG, MSA approach)	The honest GRR study (EMP approach)
Variability component	Variability component
$EV = 0.041937$	$\left(\hat{\sigma}_{pe}\right)^2 = 0.001759$
$AV = 0.011500$	$(\hat{\sigma}_o)^2 = 0.000132$
GRR = 0.043486	$(\hat{\sigma}_e)^2 = 0.001891$
$TV = 0.130196$	$(\hat{\sigma}_x)^2 = 0.016951$
$PV = 0.122719$	$\left(\hat{\sigma}_p\right)^2 = 0.015060$
% of variability component (counted as standard deviation)	% of variability component (counted as variance)
$GRR = 100 . \frac{0.043486}{0.130196} = \mathbf{33.41}$	$GRR = (\hat{\sigma}_e)^2 = 100 . \frac{0.0018902}{0.0169311} = 11.16$
$EV = 100 . \frac{0.041937}{0.130196} = 32.23$	$EV = \left(\hat{\sigma}_{pe}\right)^2 = 100 . \frac{0.001759}{0.0169311} = 10.38$
$AV = 100 . \frac{0.011500}{0.130196} = 8.81$	$AV = (\hat{\sigma}_o)^2 = 100 . \frac{0.0001315}{0.0169311} = 0.78$
$PV = 100 . \frac{0.122719}{0.130196} = 94.25$	$PV = \left(\hat{\sigma}_p\right)^2 = 100 . \frac{0.0150409}{0.0169311} = 88.84$
$ndc = 1.41 . \frac{0.122719}{0.043486} = 3.97 => \mathbf{3}$	$r_0 = \frac{0.0150409}{0.0169311} = \mathbf{0.89}$

6. CONCLUSIONS

From the submitted study, the following can be concluded:

- the total variability by the average and range method (AIAG, MSA approach) will not give the value of 100 %. The confusion here is the fact that part to part, EV & AV variations are expressed in percentage. Then there is expectation that the total variation will be 100 %.
- The honest GRR study (EMP approach) respects the basic percentage understanding and all variability components are getting the sum of 100 %. Reason for this is that the method is counting the variability components from variance.

How the perceptual components of variability are calculated by average and range method, this is explained in article [26] by Wheeler. To the fact of not getting the value of 100 % by all variability components summation (MSA approach) point also Ermer in his article [28] or Pandiripalli in his submitted thesis [20]. In general, the honest GRR study provides extended information about the measurement

system. Beyond partial variability components information, there is also information available regarding:

- process signal attenuation,
- measurement system attenuation,
- ability to detect the shift of 3 standard deviations by the subgroup of n = 10
- the ability to track the process improvement or weakness.

An interesting and recommended comparison of gauge repeatability and reproducibility methods is also available in the thesis of Stamm [19]. Nowadays, the MSA approach has a dominant position. Similar discussions are for example between the MSA and VDA5 approach. This discussion was highlighted in the article [28] by Dietrich. Also, in the case of MSA and the honest GRR study there is the fight about being the market leader for measuring system studies. And only the time will reveal the leading trend in measurement system analyses.

ACKNOWLEDGEMENT

Article has been written in connection with the project Students Grant Competition SP2017/147 and SP2017/149 financed by the Ministry of Education, Youth and Sports, and the Faculty of Mechanical Engineering VŠB-TUO.

REFERENCES

[1] Hart, R.F., Hart, K.M. (1994). The evaluation of a measurement system. *Production and Inventory Journal*, Fourth Quarter, 22-26.

[2] Antony, G.V., Knowles, G. (2000). A practical methodology for analyzing and improving the measurement system. *Quality Assurance*, 3 (3), 59-75.

[3] International Automotive Task Force. (2016). *Automotive quality management system standard. 4th Edition*. IATF16949:2016.

[4] Chrysler Corporation, Ford Motor Company, General Motors Corporation (AIAG). (1998). *Quality System Requirements. 3rd Edition*. QS-9000.

[5] Chrysler Corporation, Ford Motor Company, General Motors Corporation (AIAG). (2008). *Advanced Product Quality Planning and Control Plan (APQP), Second Edition*. AIAG.

[6] Hermans, J.E., Liu, Y. (2013). Quality management in the new product development: A PPAP approach. *Quality – Innovation - Prosperity*, 17 (2).

[7] Chrysler Corporation, Ford Motor Company, General Motors Corporation (AIAG). (2010). *MSA - Measurement Systems Analysis (MSA), Fourth Edition*. AIAG.

[8] Wheeler, D.J. (2006). *EMP III - Evaluating the Measurement Process & Using Imperfect Data*. SPC PRESS (Statistical Process Control).

[9] Verband der Automobileindustrie e.V. (2011). *VDA 5 – Vhodnost kontrolních procesů, 2. vydanie*. Praha, ČR: Česká společnost pro jakost.

[10] Klaput, P. (2014). *Methodical approach to measurement system analyses*. Dissertation Thesis, VŠB - Technical University of Ostrava, Faculty of Metallurgy and Materials Engineering. (in Czech)

[11] Dietrich, E., Schulze, A. (2003). *Eignungsnachweis von Prüfprozessen*. Carl Hanser Verlag.

[12] Kazerouni, A.M. (2009). Design and analyses of gauge R&R studies: Making decision based on ANOVA method. *International Journal of Mechanical, Aerospace, Industrial, Mechatronic and Manufacturing Engineering*, 3 (4).

[13] Throne, J.L. (2008). *Understanding Thermoforming*. Carl Hanser Verlag.

[14] Rolls-Royce (2013). *Measurement System Analyses : How-to Guide. Version 6.1*. Rolls-Royce plc., 53.

[15] Healy, S., Wallace, M. (2011). Gage repeatability and reproducibility methodologies suitable for complex test systems in semi-conductor manufacturing. In *Six Sigma Project and Personal Experiences*. InTech.

[16] Minitab. (2010). *Minitab guideline of methods and formulas. Version 16.1.1.0*. Minitab Inc.

[17] Knowles, G., Vickers, G., Anthony, J. (2003). Implementing evaluation of the measurement process in an automotive manufacturer: A case study. *Quality and Reliability Engineering International*, 19 (5), 397-410.

[18] Dusharme, D. (2011). *An Interview with Donald J. Wheeler*. Quality Digest, May 2011.

[19] Stamm, S. (2013). *A comparison of gauge repeatability and reproducibility methods*. Dissertation Thesis, Indiana State University, USA.

[20] Pandiripalli, B. (2010). *Repeatability and reproducibility studies: A comparison of techniques*. Thesis, Wichita State University, USA.

[21] SAS Institute. (2013). *SAS/QC 13.1 : User´s Guide*. Cary, NC, USA: SAS Institute Inc.

[22] BPI Consulting, LLC. (2014). *Evaluating the Measurement Process - Part 1*.

[23] Wheeler, D.J. (2009). An honest gauge R&R study (rev.). In *ASQ/ASA Fall Technical Conference*, Manuscript No. 189.

[24] Wikimedia Foundation, Inc. *Western electric rules*. https://commons.wikimedia.org/wiki/File:Western_electric_rules.svg.

[25] Wachs, S. *How can an OC curve be used to manage the risk of undetected special causes?* http://www.integral-concepts.com/docs/.

[26] Wheeler, D.J. (2016). *Good data, bad data, and process behaviour charts*. http://asq.org/statistics/2003/01/good-data-bad-data-and-process-behavior-charts.pdf.

[27] Ermer, S.D. (2016). Improved gage R&R measurement studies. *Quality Progress*, March 2006, 77-79.

[28] Dietrich, E. (2011). Wo liegen die Unterschiede? Vergleich von MSA and VDA Band 5. *QZ*, 56 (6), 30-34. http://vda-qmc.de/fileadmin/redakteur/presse/QZ6_11_Vergleich_von_MSA_und_VDA_Band_5.pdf.

[29] Standards Department VW. (2012). *Capability of measuring processes (Consideration of measuring uncertainty in test processes)*. Standard VW 10119.

[30] Krolczyk, J., Krolczyk, G., Legutko, S., Napiorkowski, J., Hloch, S., Foltys, J., Tama, E. (2015). Material flow optimization – a case study in automotive industry. *Tehnički vjesnik – Technical Gazette*, 22 (6), 1447-1456.

[31] Nieslony, P., Krolczyk, G.M., Wojciechowski, S., Chudy, R., Zak, K., Maruda, R.W. (2018). Surface quality and topographic inspection of variable compliance part after precise turning. *Applied Surface Science*, 434, 91-101.

Received October 10, 2017.
Accepted February 14, 2018.

MEASUREMENT SCIENCE REVIEW, **18**, (2018), No. 1, 28-34

DE GRUYTER OPEN

MEASUREMENT SCIENCE REVIEW

Journal homepage: http://www.degruyter.com/view/j/msr

ISSN 1335-8871

Theoretical Analysis of the Rectangular Defect Orientation using Magnetic Flux Leakage

J. Sam Alaric[1], V. Suresh[2], A. Abudhahir[3], M. Carmel Sobia[4], M. Baarkavi[5]

[1]*Wollega University, Department of Electrical and Electronics Engineering, Ethiopia*
[3]*VEL TECH Dr.RR & Dr. SR Technical University, Chennai 600 062, India*
[2,4,5] *National Engineering College, Electronics and Instrumentation Engineering Department, Kovilpatti, 628503, Tamilnadu, India, vseie@nec.edu.in*

This paper presents an approach to estimate the orientation of the rectangular defect in the ferromagnetic specimen using the magnetic flux leakage technique. Three components of the magnetic flux leakage profile, such as radial, axial, and tangential component are considered to estimate the orientation of the rectangular defect. The orientation of the rectangular defect is estimated by the proposed analytical model using MATLAB software. The results calculated by the analytical model are validated by the three-dimensional finite element analysis using COMSOL Multiphysics software. Tangential component provides better performance to estimate the orientation of the rectangular defect compared with radial and axial component of the magnetic flux leakage profile.

Keywords: Magnetic flux leakage, orientation of the defect, radial component, axial component, tangential component, finite element analysis.

1. INTRODUCTION

Magnetic Flux Leakage (MFL) technique is a well-established Non-Destructive Testing (NDT) method to detect the surface and subsurface defects in the ferromagnetic material. The basic principle of the MFL is that a specimen under inspection is magnetized near saturation under the applied magnetic field. If there is no defect on the specimen, the majority of the magnetic flux lines pass through the specimen material itself, in contrast, the leakage field is created due to the smaller permeability in the defect region [1]-[4]. Three major vector components of the leakage profile are radial, axial, and tangential. The geometry of the defect and its dimension may change the pattern of the three components [5], [6]. Forward and Inverse approach are referred to in the MFL inspection technique. Dipole based analytical model and finite element based numerical model provide the solution for a forward approach. In this work, forward approach is considered to detect the orientation of the rectangular shaped defect. In forward approach, the MFL testing is performed in the calibrated sample with a known defect and the pattern of the leakage profile is recorded. The data obtained through the in-situ inspection of the specimen in literature are compared with the MFL profile generated by the calibrated samples. Recording the pattern of the leakage profile for the known defect in forward approach is not necessary when the dipole model is considered [2], [7]. Zatsepin et al. (1966) introduced an analytical model using the point or strip of dipole for rectangular shape defect [8]. The magnitude of the leakage profile and the externally applied field are not considered. Later on, Shcherbinin et al. (1972) extended the Zatsepin model by considering the 3-D rectangular shape defect with finite size. The maximum amplitude of the radial and axial components of leakage profile in the symmetry axis was considered and the size of the defect was not discussed. [9]. Forster et al. (1986) improved the model of Shcherbinin for the same type of defect by considering the magnitude of the applied field and magnetic property of the specimen [10]. Minkov et al. (2002) applied the dipolar model to 3-D rectangular defect and reported that the strength of the radial component leakage profile is directly proportional to the depth of the defect [11]. Sushant.
Dutta et al. (2009) proposed a 3-D analytical model for surface breaking in ferromagnetic specimen which has a maximum magnitude for radial component rather than for axial and tangential. Leakage signal prediction and defect characterization were also performed using the analytical model [12]. Maryam Ravan et al. (2010) developed an analytical model for the arbitrary defect sizing. The main drawback of that method is longer computation time [13]. Wenhua Han et al. (2014) developed an algorithm to estimate the two-dimensional defect in fast manner and the length of the defect is not considered [14]. Dipole model was developed to measure the alternating magnetic field

DOI: 10.1515/msr-2018-0005

created for circular type defect in the titanium alloy pipe. The eddy current principle is used in this study. Distorted eddy current in the defect region generates the alternating magnetic field in the radial direction of the pipeline. Volumetric studies are performed to validate the analytical model along with the finite element method and experimental method [4]. Analytical model for the radial component of the leakage profile is proposed and lift-off study is also performed. Estimation of the defect from analytical model is correlated with the actual defect parameter. Performance of the analytical model is validated through experimental results [5]. The performance of the radial and axial component of non-orientated rectangular defect is analyzed and we conclude that the radial component provides excellent performance to estimate the length and depth of the defect [15]. COMSOL Multiphysics software is employed to estimate the crack depth using alternating current potential drop technique [16]. The effect of defect orientation of the steel plates was studied and the influence of the orientation was estimated in terms of crack propagation [17].

In general, the rectangular defect was presented with orientation on the specimen. In this research work analytical model is proposed to estimate the orientation of the rectangular defect using the three components of the leakage profile. Among the three components, tangential component provides the good performance to estimate the orientation of the defect. For validation, the finite element studies are performed by using COMSOL Multiphysics software.

2. ANALYTICAL MODEL FOR THREE COMPONENTS OF MFL

Fig.1. shows the rectangular shape defect on the steel slab with the notation of length '2 l', width '2 w', and depth 'd'. The angle between the discontinuity orientation and magnetization direction is represented by 'β'.

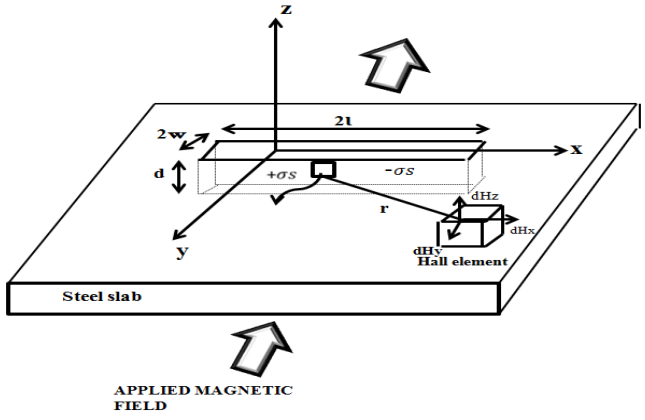

Fig.1. Dipolar representation of rectangular defect.

Three components of the leakage profile are represented as axial component 'B_x', tangential component 'B_y', and radial component 'B_z'. The orientation of the defect may affect the three components of the leakage profile. The Axial (x´), tangential (y´), and radial (z´) component of the magnetic field at a point with coordinates x´, y´, and z´ is given by

$$B_{x'}(\beta) = \frac{sin^2\beta\sigma_{ms}}{2\pi\mu_\circ}$$

$$\begin{bmatrix} arctan\dfrac{d(x'sin\beta + b)}{(x'sin\beta + b)^2 + z'(z' + d)} \\ -arctan\dfrac{(xsin\beta - b)}{(x'sin\beta - b)^2 + z'(z' + d)} \end{bmatrix} \quad (1)$$

$$B_{y'}(\beta) = \frac{sin\beta cos\beta\sigma_{ms}}{2\pi\mu_\circ}$$

$$\begin{bmatrix} arctan\dfrac{d(x'sin\beta + b)}{(x'sin\beta + b)^2 + z'(z' + d)} \\ -arctan\dfrac{(xsin\beta - b)}{(x'sin\beta - b)^2 + z'(z' + d)} \end{bmatrix} \quad (2)$$

$$B_{z'}(\beta) = \frac{sin\beta\sigma ms}{4\pi\mu_\circ}$$

$$\begin{bmatrix} ln\dfrac{(x'sin\beta + b)^2 + (z' + d)^2}{(x'sin\beta - b)^2 + (z' + d)^2} \\ +ln\dfrac{(x'sin\beta - b)^2 + z'^2}{(x'sin\beta + b)^2 + z'^2} \end{bmatrix} \quad (3)$$

To analyze the MFL signal characteristics of the discontinuity in a different orientation, the length 2 l, the width 2 w, depth d, lift-off z´, and $\sigma_{ms}/4\ \pi\mu$ were assumed to be 2 cm, 1.5 cm, 0.50 cm, 1 mm and 1, respectively. The $B_{x'}(\beta)$, $B_{y'}(\beta)$, and $B_{z'}(\beta)$ are calculated for the orientation angle β from 0 to 90 degrees.

From Fig.2. it is observed that the magnitude of the three components of the MFL signal varied for the different orientations of the defect. The defect orientation angle β is increased from 0 to 90 degrees and the analytical model output is observed. The amplitude of the axial and radial component is increased and very minor magnitude changes in the 75, 80 and 90-degree orientation are observed. The amplitude of the tangential component is first increased from 0 to 45-degree orientation and then decreased from 45 to 90 degrees. Polynomial expression for axial, radial, and tangential component of the leakage profile is derived using the magnitude of the leakage profile. Tangential component has two polynomial expressions, the expression (6a) is used to estimate the orientation from 0 to 45 degrees and the expression (6b) is used to estimate the orientation from 46 to 90 degrees.

$$axial\ angle = 33B_x^3 - 69B_x^2 + 107B_x + 3 \quad (4)$$

$$radial\ angle = 2B_z^3 - 6B_z^2 + 21B_z + 1 \quad (5)$$

$$tangential\ angle = -242B_y^3 + 286B_y - 74 \quad (6a)$$

$$tangential\ angle = 222B_y^3 + 286\,B_y^2 - 28B_y + 90 \quad (6b)$$

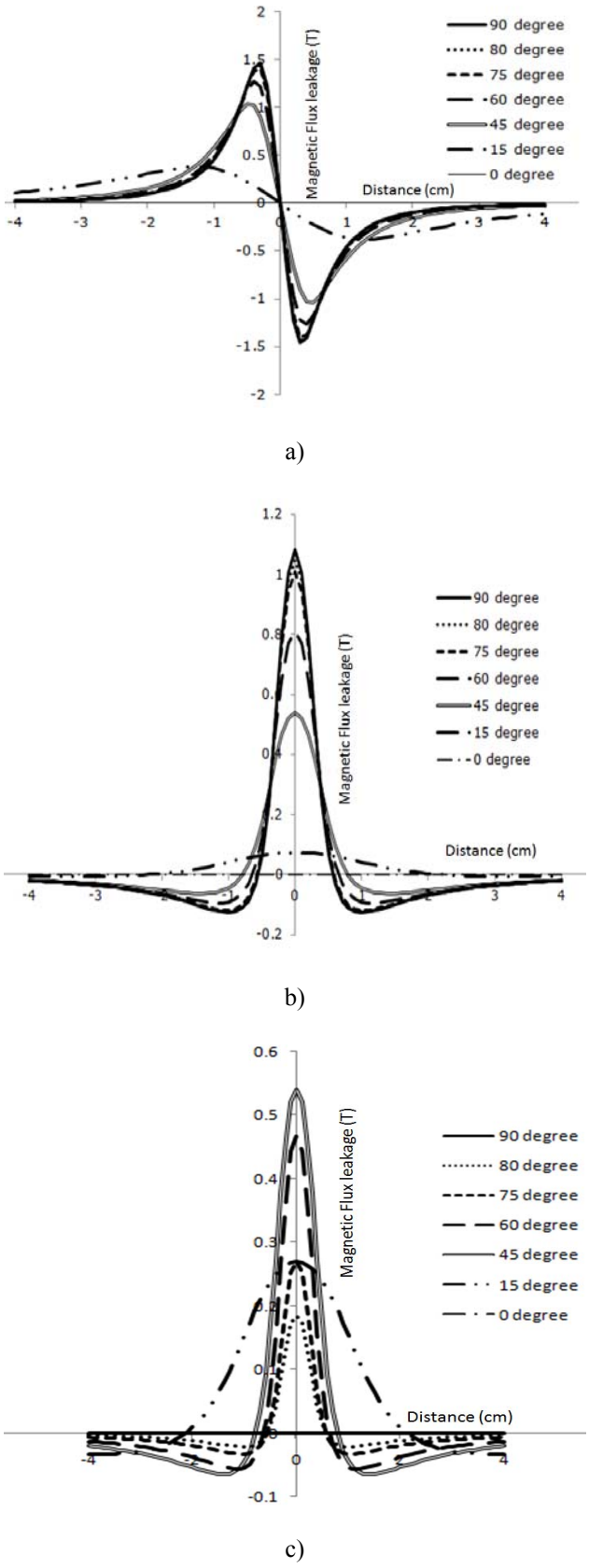

Fig.2. MFL profile of analytical model output for the different orientation of discontinuity
a) Axial profile, b) radial profile, c) tangential profile.

Error percentage of the three components of the MFL profile during the estimation of the angle is shown in Table 1. The average error percentage of the radial and axial leakage profile component is '13' and '7'. When comparing axial and radial component, the axial component has less average error percentage. It is observed that the radial component failed to estimate the orientation of the defect. Among the three components, tangential leakage profile provides better estimation. Axial and tangential components are considered to estimate the defect orientation in numerical studies.

Table 1. Estimated error % for orientation of three profiles.

Actual angle (degree)	Estimated angle for Axial (degree)	Estimated angle for Radial (degree)	Estimated angle for Tangential (degree)	Error (%) for Axial profile	Error (%) for Radial profile	Error (%) for tangential profile
15	10	17	15	33	46	0
45	47	39	45	4	13	0
60	60	67	60	0	11	0
75	71	78	75	5	4	0
80	81	79	80	1	1	0
90	89	82	90	1	8	0

3. NUMERICAL MODEL FOR TANGENTIAL AND AXIAL COMPONENT OF MFL

The finite element approach is an efficient method to identify the defect on the inspected specimen. Three-dimensional finite element studies are performed to validate the proposed analytical model. COMSOL Mutiphysics 4.3a modeling software is utilized to implement the finite element analysis. AC/DC module of the software is facilitated to compute the electric and magnetic field analysis on the inspected specimen. Fig.3. shows the three-dimensional geometry of 15-degree oriented rectangular defect on the rectangular ferromagnetic steel slap with permanent magnet. The length, width and thickness of the ferromagnetic steel slab are 100 cm x 100 cm x 15cm. The rectangular defect is of length 50 cm, width 5 cm and depth 7.5 cm with 15, 45 and 80-degree orientations. Two permanent magnets are used to magnetize the inspected specimen. The entire arrangement is surrounded by the air bounded domain.

Table 2. shows the domain specification of ferromagnetic plate and the permanent magnet in COMSOL Multiphysics 4.3a.

In the preprocessing of the geometry, tetrahedral element is considered for meshing operation. Fig.4. shows the tetrahedral meshed geometry of the specimen with the help of 131,338 elements and 838,650 numbers of degrees of freedom. Computation time taken for this preprocessing is 72 seconds.

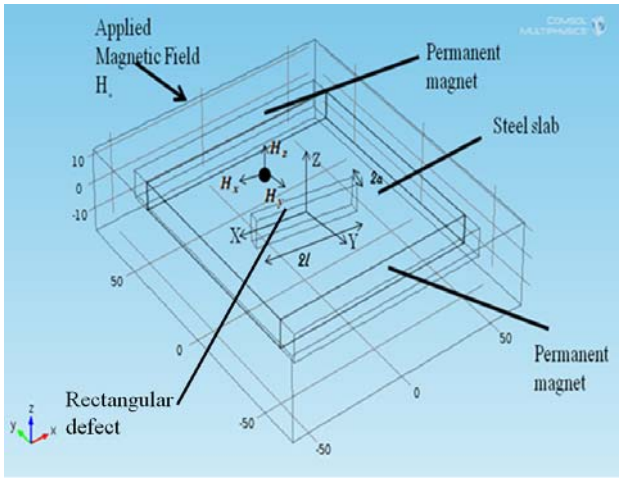

Fig.3. Geometry of the specimen with defect.

Table 2. Domain specification of the model.

Specification	Ferromagnetic Plate	Permanent Magnet
Material	ASTM A213-76a, Grade T9 (9Cr-1Mo)	Neodymium
Relative permittivity	1	1
Electrical conductivity [S/m]	4.032e6	sigma_solid_1 (T[1/k])
Relative permeability	100	4000

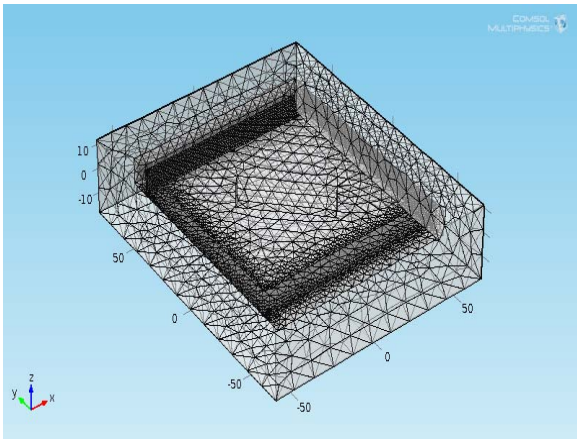

Fig.4. Meshed geometry of the specimen with defect.

The property of the mesh considered for this finite element analysis is shown in Table 3.

Table 3. Properties of mesh.

Element size parameter	Value
Max element size	12
Min element size	1.5
Max element growth rate	1.45
Resolution of curvature	0.5
Resolution of narrow regions	0.6

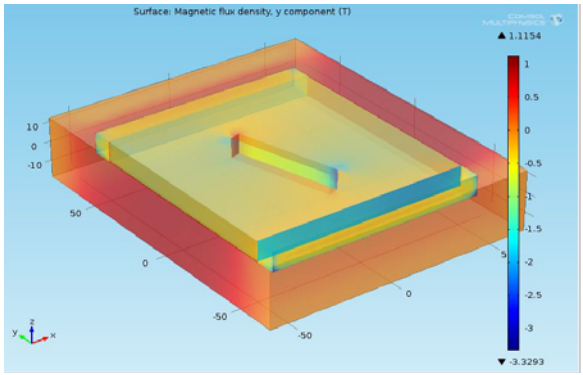

a) 15-degree orientation

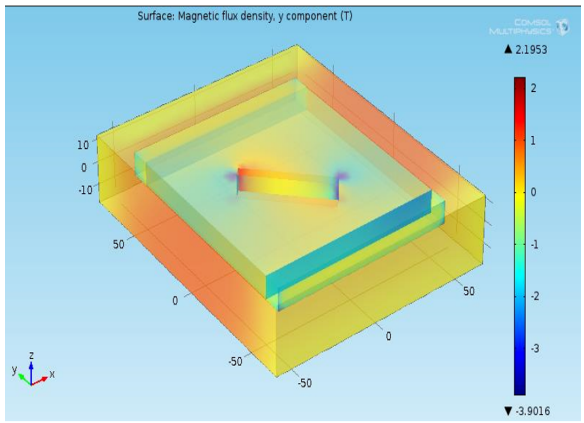

b) 45-degree orientation

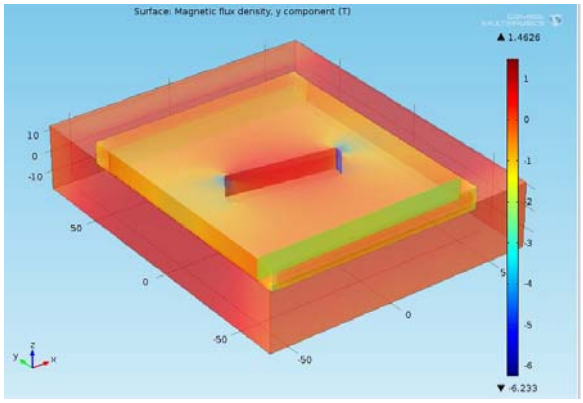

c) 80-degree orientation

Fig.5. Surface plots of the tangential component for different orientations of the defect.

In the AC/DC module of COMSOL Multiphysics software, the stationary solver study is performed on the developed geometry. In post processing of the solved geometry the surface plot is constructed. Fig.5. shows the surface plot of 15, 45 and 80-degree orientation of the defect. The uniform distribution of the magnetic field in the entire region of the specimen and the variation of the leakage profile in the defect region shows the effective arrangement of permanent magnet along with the inspected specimen. The stepwise single point line scan is performed for 100 cm length of the specimen and the magnitude of the axial and tangential component of the leakage profile is observed.

4. RESULTS AND DISCUSSION

To validate the proposed analytical model a comparison study is performed between the outputs of analytical model with numerical model. The dimension of the defect in the comparison study is considered to be of length 50 cm, width 5 cm, and depth 7.5 cm. The orientation of the defect with respect to the applied magnetic field is 15 degrees, 45 degrees, and 80 degrees. Fig.6. shows the normalized output of the axial and tangential component of the analytical model. Normalization of the magnetic leakage profile output does not affect the defect information [2]. The magnitude of the axial component decreases while the orientation of the defect increases. In the case of tangential component, the magnitude is increased from 0 to 45 degrees of orientation and then the magnitude of the profile is decreased up to 90 degrees of orientation.

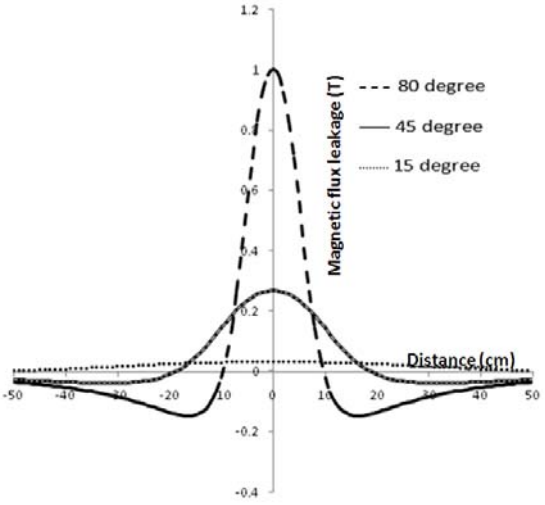

a)

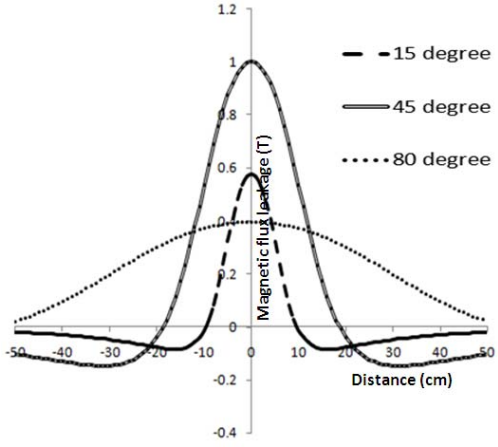

b)

Fig.6. Analytical output for different orientation
a) axial component, b) tangential component.

The polynomial expression is derived using the actual angle with the corresponding analytical output magnitude of the leakage field. The equation (7) is derived with the help of axial profile magnitude and the equation (8) is derived with the help of tangential profile magnitude. Error percentage of the angle estimation for the axial and tangential component of the analytical model output is shown in Table 4.

$$axial\ angle = -145B_x^3 + 208B_x^2 + 24B_x - 1 \quad (7)$$

$$tangential\ angle = B_y^3 + 29\,B_y^2 - 8B_y + 1 \quad (8a)$$

$$tangential\ angle = -238B_y^3 + 182\,B_y^2 - 74B_y + 90 \quad (8b)$$

Table 4. Estimated error % for analytical model.

Actual angle (degree)	Estimated angle for Axial (degree)	Estimated angle for Tangential (degree)	Error (%) for Axial component	Error (%) for Tangential component
15	21	15	28	0
45	41	45	8	0
80	82	80	2	0

Fig.7. shows the normalized output of the axial and tangential component of numerical model. The magnitude of the leakage profile of both components in numerical model is varied as discussed in the analytical model output. The polynomial expression is derived using the actual angle with the corresponding numerical output magnitude of the leakage field.

$$axial\ angle = 9B_x^3 - 46B_x^2 + 79B_x - 2 \quad (9)$$

$$tangential\ angle = 67B_y^3 - 88\,B_y^2 + 67B_y + 0 \quad (10a)$$

$$tangential\ angle = -39B_y^3 - 12\,B_y^2 - 53B_y + 90 \quad (10b)$$

Error percentage of the angle estimation for the axial and tangential component of the numerical model output is shown in Table 5.

Table 5. Estimated error % for numerical model.

Actual angle (degree)	Estimated angle for Axial (degree)	Estimated angle for Tangential (degree)	Error (%) for Axial component	Error (%) for Tangential component
15	18	15	20	0
45	42	45	5	0
80	83	80	3	0

The tangential component provides the minimum error percentage when compared to the axial component in analytical and numerical model output. The orientation of the defect on the ferromagnetic specimen is estimated accurately using the tangential component of the MFL profile.

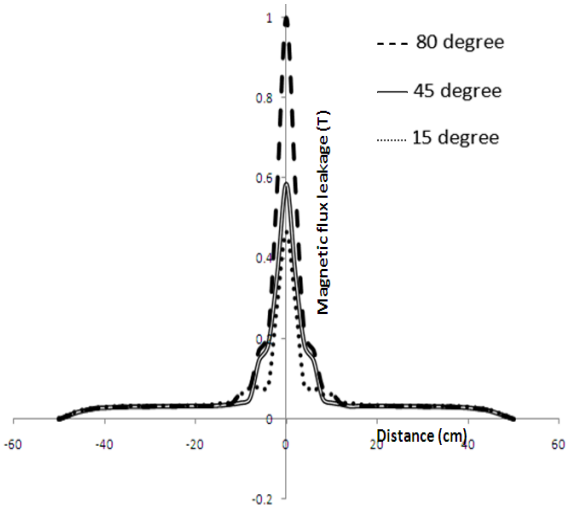

a)

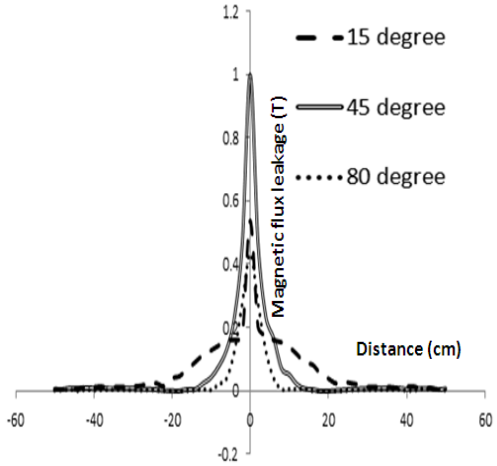

b)

Fig.7. Numerical output for different orientation
a) axial component, b) tangential component.

5. CONCLUSION

We have developed an analytical model to estimate the orientation of the defect in ferromagnetic specimen. The result of the analytical model analysis showed that the radial component has large error to estimate the angle of the defect, and hence, the axial and tangential components are considered in the numerical study. The tangential component measured the defect orientation in precise manner when compared to the axial component. For validation purpose the numerical studies are performed using COMSOL Multiphysics software. Good correlation among the analytical and numerical studies revealed the good performance of the proposed method. The most important step of the forward approach, such as recording the pattern of the leakage profile for the known defect, is eliminated by using the proposed analytical model and also the proposed model provides support to reconstruct the defect in the inverse MFL problem.

ACKNOWLEDGMENT

The authors would like to thank Prof. Jackson Daniel for technical discussion and also thank Prof. Shankar for language correction.

REFERENCES

[1] Rao, B.P.C. (2012). Magnetic flux leakage. *Journal of Non - Destructive Testing & Evaluation*, 11 (3), 7-17.

[2] Mandache, C., Clapham, L. (2003). A modelfor magnetic flux leakage signal predication. *Journal of Physics D: Applied Physics*, 36, 2427-2431.

[3] Jianbo, W., Yanhua, S., Yihua, K., Yun, Y., (2015). Theoritical analyses of MFL signal affected by discontinuity orientation and sensor scanning direction. *IEEE Transactions on Magnetics*, 51 (1).

[4] Le, M., Lee, J., Junc, J., Kima, J. (2013). Estimation of sizes of cracks on pipes in nuclear power plants using dipole moment and finite element methods. *NDT & E International,* 58, 56-63.

[5] Suresh, V., Abudhahir, A., (2016). An analytical model for prediction of magnetic flux leakage from surface defects in ferromagnetic tubes. *Measurement Science Review*, 16 (1), 8-13.

[6] Suresh, V., Abudhahir, A., Jackson, D., (2017). Development of magnetic flux leakage measuring system for detection of defect in small diameter steam generator tube. *Measurement*, 95, 273-279.

[7] Mandache, C., Shiari, B., Clapham, L. (2005). Defect separation considerations in magnetic flux leakage inspection. *Insight,* 47 (5), 269-273.

[8] Zatsepin, N.N., Shcherbinin, V.E. (1966). Calculation of the magnetostatic field of surface defects. *Defektoskopiya*, 5, 50-59.

[9] Shcherbinin, V.E., Pashagin, A. (1972). Influence of the extension of a defect on the magnitude of its magnetic fields. *Defektoskopiya*, 8, 72-83.

[10] Forster, F. (1986). New findings in the field of non destructive magnetic leakage field inspection. *NDT International*, 19 (1), 3-14.

[11] Minkov, D., Takeda, Y., Shoji, T., Lee, J. (2002). Estimating the sizes of surface cracks based on Hall element measurements of the leakage magnetic field and a dipole model of a crack. *Applied Physics A*, 74 (2), 169-176.

[12] Dutta, S.M., Ghorbel, F.H., Stanley, R.K. (2009). Dipole modeling of magnetic flux leakage. *IEEE Transactions on Magnetics*, 45 (4), 1959-1965.

[13] Ravan, M, Amineh, R.K, Koziel, S, Nikolova, N.K., Reilly, J.P. (2010). Sizing of 3-D arbitrary defects using magnetic flux leakage measurements. *IEEE Transactions on Magnetics*, 46 (4), 1024-1033.

[14] Han, W., Shen, X., Xu, J., Wang, P., Tian, G., Wu, Z. (2014). Fast estimation of defect profiles from the magnetic flux leakage signal based on a multi-power affine projection algorithm. *Sensors*, 14 (9), 16454-16466.

[15] Suresh, V., Abudhahir, A. (2016). Dipole model to predict the rectangular defect on ferromagnetic pipe. *Journal of Magnetics*, 21 (3), 437-441.

[16] Yuting, L., Fangji, G., Zhengjun, W., Junbi, L., Wenqiang, L. (2015). Novel method for sizing metallic bottom crack depth using multi-frequency alternating current potential drop technique. *Measurement Science Review*, 15 (5), 268-273.

[17] Aljabar, N.J., Zhao, X.L., Al-Mahaidi, R., Ghafoori, E., Motavalli, M., Powers, N. (2016). Effect of crack orientation on fatigue behavior of CFRP-strengthened steel plates. *Composite Structures*, 152, 295-305.

Received November 16, 2017.
Accepted February 15, 2018.

MEASUREMENT SCIENCE REVIEW, **18**, (2018), No. 1, 35-40

DE GRUYTER OPEN

MEASUREMENT SCIENCE REVIEW

Journal homepage: http://www.degruyter.com/view/j/msr

ISSN 1335-8871

Testing an Impedance Non-destructive Method to Evaluate Steel-Fiber Concrete Samples

Tereza Komarkova[1], Pavel Fiala[2], Miloslav Steinbauer[3], Zdenek Roubal[3]

[1] *Department of Building and Testing, Faculty of Civil Engineering, BUT, Veveri 95, 602 00, Brno, Czech Republic, tereza.komarkova@vutbr.cz*

[2] *SIX Centre, FEEC, BUT, Technická 3082/12, 616 00, Brno, FEEC, BUT, Technicka 3082/12, 616 00 Brno; Czech Republic*

[3] *Department of Theoretical and Experimental Electrical Engineering, FEEC, BUT, Technicka 3082/12, 616 00, Brno; Czech Republic*

Steel-fiber reinforced concrete is a composite material characterized by outstanding tensile properties and resistance to the development of cracks. The concrete, however, exhibits such characteristics only on the condition that the steel fibers in the final, hardened composite have been distributed evenly. The current methods to evaluate the distribution and concentration of a fiber composite are either destructive or exhibit a limited capability of evaluating the concentration and orientation of the fibers. In this context, the paper discusses tests related to the evaluation of the density and orientation of fibers in a composite material. Compared to the approaches used to date, the proposed technique is based on the evaluation of the electrical impedance Z in the band close to the resonance of the sensor–sample configuration. Using analytically expressed equations, we can evaluate the monitored part of the composite and its density at various depths of the tested sample. The method employs test blocks of composites, utilizing the resonance of the measuring device and the measured sample set; the desired state occurs within the interval of between f=3 kHz and 400 kHz.

Keywords: Steel-fiber; concrete; non-destructive testing; electromagnetic field; electric impedance.

1. INTRODUCTION

The last decades have witnessed major development of fiber-reinforced concrete, a material formed through the addition of a metal reinforcement (filler), but also the general rise of interest in composite materials and related non-destructive testing methods [1]-[7].

In order for a material to exhibit the required mechanical and thermal properties, it is necessary to ensure the related macroscopic properties, such as the homogeneous and isotropic distribution of the components, and thus also the resulting parameters. This phase depends on selecting a suitable technology to prepare and manufacture the given material. Intensive attention is thus paid to methods and principles that enable us to evaluate non-destructively the concentration of the components of a composite, fillers in particular; by extension, these approaches are also employed to assess the orientation of individual elements in a concrete filler [6], [8]-[10]. An interesting tool consists of techniques and devices to evaluate the concentration of fibrous particles, or steel fibers, in both fresh and solidified concrete; in this case, however, the orientation of the fibers can be assessed only with considerable difficulty.

The presently used techniques exploit the common evaluation of the electrical impedance Z of the tested sample [4], [5], and they employ dedicated experiments to derive the relationship between changes of the module of the electrical impedance Z and orientation of the steel fibers. Generally, researchers point out the relationship between the impedance magnitude and the concentration of the fibers.

Our experiments have shown that, utilizing the electric and ferromagnetic properties of steel fibers as the composite filler component in reinforced concrete, it is possible to monitor the concentration and distribution of the fibers in a non-destructive manner [1]. Further, the use of a suitable measurement methodology and the frequency band close to the resonance of the sensor–sample configuration facilitates more accurate derivation and evaluation of the composition of the monitored composite component, namely, the steel fibers [1], [13].

2. THE IMPEDANCE MEASURING METHOD AND THE NEAR-RESONANCE STATE

The non-destructive methods presented to date, such as those discussed in papers [11]-[12], exploit the properties of the electromagnetic (EMG) field to monitor the distribution

DOI: 10.1515/msr-2018-0006

of fibers in the tested composite. To evaluate the properties of the composite components, the actual principle employs the electric impedance $\hat{Z}$ in the region of the monitored sample; we can then write

$$\hat{Z} = \frac{\left|\hat{\boldsymbol{E}}\right|}{\left|\hat{\boldsymbol{H}}\right|} \ , \tag{1}$$

where $\hat{Z}$ denotes the complex impedance of the harmonic behavior of the electric and magnetic field components, $\hat{\boldsymbol{E}}$ is the complex vector of the electric field intensity, and $\hat{\boldsymbol{H}}$ denotes the complex vector of the magnetic field intensity. The details of the fields and other aspects are shown in, for example, Fig.1. The frequency f of the impedance meter's excitation signal (Fig.1.) is progressively set such that the resonance quality factor Q_{h} could assume the values

$$Q_{0.5} = \frac{1}{2}Q_{\boldsymbol{max}} \ , \quad Q_{sq2} = \frac{1}{\sqrt{2}}Q_{\boldsymbol{max}} \ , \quad Q_{sq3} = \frac{1}{\sqrt{3}}Q_{\boldsymbol{max}} \tag{2}$$

In the experimental setting, the values proved to be beneficial for the final evaluation of the location with non-uniform distribution of the composite material components. To evaluate the mass density of the monitored composite material component, the electric power specific density (the Poynting vector) is assessed; this vector is then written as

$$\hat{\boldsymbol{\Pi}} = \hat{\boldsymbol{E}} \times \hat{\boldsymbol{H}} \ , \tag{3}$$

where the symbol × denotes the vector product.

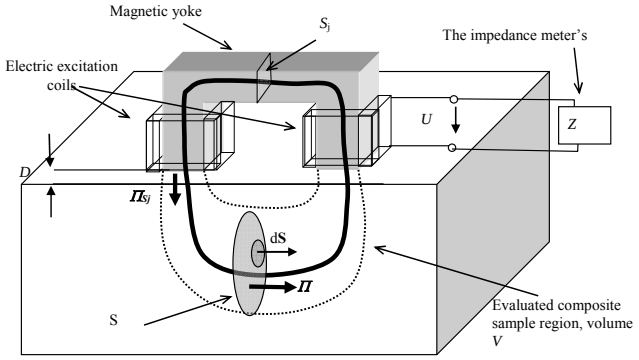

Fig.1. A scheme of the impedance-based NDT method: the evaluation of the tested sample parameters.

The dissipated electrical power P generated in the monitored composite material component is bound to the surface density of the active power $\hat{\boldsymbol{\Pi}}$ from the above expression (3), and this dissipated power is formulated within

$$P = \int_{S_j} \boldsymbol{\Pi}_{S_j} \cdot d\,\boldsymbol{S} \quad , \tag{4}$$

where P is the dissipated electrical power in the region having the volume V in the measured portion of the composite material, $\boldsymbol{\Pi}_{S_j}$ denotes the power flux surface density in the area of the shaping yoke at the distance D from the surface of the composite material, d$\boldsymbol{S}$ is the vector of the element of the cross section area of the measured part of the composite material sample, S_{j} represents the section through the magnetic yoke, and S is the cross section of the area of the monitored material sample (Fig.1.).

In relation to the preset resonant frequency f_{r} of the entire setup comprising a detection and measuring device and an electric coil wound on the arms of a ferromagnetic yoke, we have – for the complex impedance $\hat{Z}$ in the exponential form – the formula

$$\hat{Z}_0\Big|_{f_r} = \frac{\left|\hat{\boldsymbol{E}}\right|}{\left|\hat{\boldsymbol{H}}\right|} \angle\varphi_0 \ , \varphi_0 \cong 0 \quad . \tag{5}$$

For the component form, the complex impedance is written as

$$\hat{Z}_0\Big|_{f_r} = Z_{0,\boldsymbol{Re}} + jZ_{0,\boldsymbol{Im}} \ , \forall f = f_r \ \textit{holds} \ Z_{0,\boldsymbol{Im}} \cong 0 \quad , \tag{6}$$

where $Z_{0,\mathrm{Re}}$, $Z_{0,\mathrm{Im}}$ are the real and imaginary components of the complex impedance $\hat{Z}$. Based on such measured data, it is then easy to evaluate the magnitude of the dissipated power (3), which corresponds to the mass density of the monitored composite material component

$$P = \mathrm{Re}\left\{\frac{U^2}{\hat{Z}_0}\right\} \ , \tag{7}$$

where U is the effective value (RMS) of the electric voltage on the terminals of the excitation coils in Fig.1.

The change of resonance for the initial preset frequency f_{r} of the detection and measuring device and the connected electric coil will occur if the position of the ferromagnetic yoke is altered such that, in the monitored volume V of the tested composite material sample, we can observe a variation of the mass density ρ or the orientation of the needle-like formations of the monitored composite material components.

Using the above-expressed relationships between the mass density of the composite material component and the electromagnetic field, (3) to (7), it is possible to evaluate the parameters of the desired properties of the composite material samples according to the function g:

$$U^2 = g\left(J^2, \gamma_{ef}^2, S(f)\right) \quad , \tag{8}$$

where J is the current density in the volume V, and γ_{ef} denotes the equivalent specific electrical conductivity in the volume V, Fig.1.

3. EVALUATING THE TESTS OF BLOCKS AND PARAMETERS

The proposed methodology tests [13] were performed in laboratory conditions, Fig.2. The actual testing of the composite material sample (with the applied needle-like filler components, Fig.3., Fig.4., and Fig.5.) for the selected type and version of the magnetic yoke within the given frequency range is shown in Fig.6.

To enable the testing and evaluation of the specific density of the monitored parts of the composite ρ (Fig.5.) in the block of the sample (Fig.3.), we assessed the losses dP [W] in the measured area as having volume V. In the sample P4 from Fig.3., given the frequency of f_r=328.630 kHz, we determined the losses of dP_{co}= 39.1 μW and dP_{fi}=37.0 mW on the fine and coarse sides (Δx_{fi}<0.2 mm and $\Delta x_{co}\cong$10 mm, respectively). The reference structures lacking metal elements of the composite, dP_{fant} = 0.349 mW, and the composite distribution characteristics were analyzed differently (Fig.7., Fig.8., and Fig.11.). A similar test was performed for the same sample at the frequency of f_r=146.000 kHz, again involving both the fine (Δx_{fi}<0.2 mm) and the coarse ($\Delta x_{co}\cong$10 mm,) sides; the relevant evaluated losses corresponded to dP_{co}=30.6 mW and dP_{fi}=36.6 mW. The reference structures lacking metal elements of the composite exhibited the value of dP_{fant} = 22.8 mW (Fig.9., Fig.10., and Fig.12.).

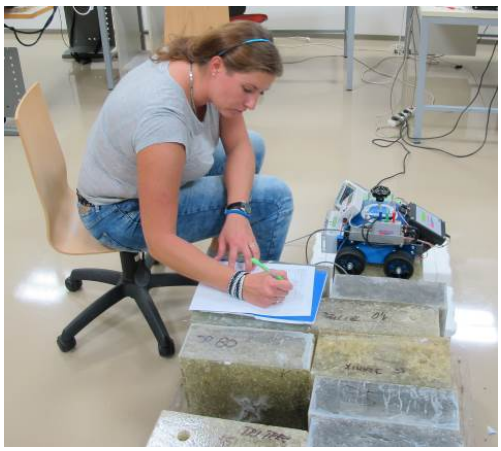

Fig.2. The measuring test system and recording device (NDT) to evaluate the impedance module/phase of the monitored component at the DTEEE laboratories.

Fig.3. The composite material sample (P4) tested at the DTEEE laboratories; the dimensions are 300x300x140 mm.

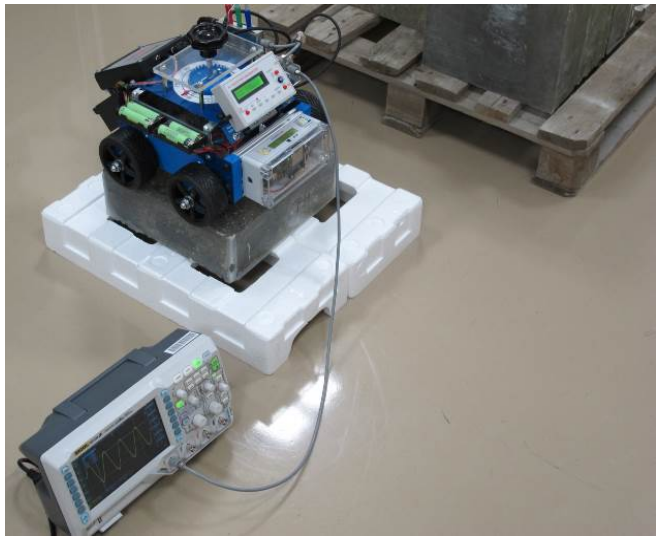

Fig.4. The compact NDT measurement and recording device to evaluate the impedance module/phase of the monitored component of the composite material sample. The apparatus operates as a semi-automatic monitoring system.

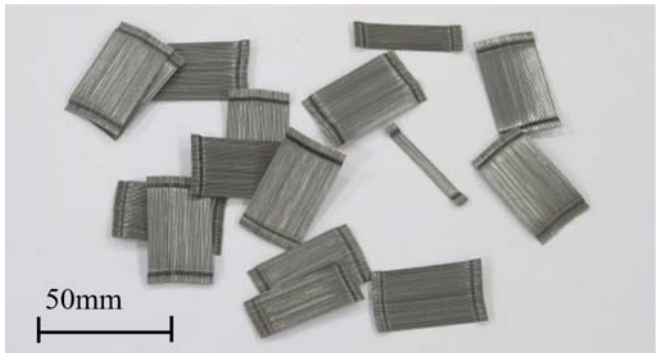

Fig.5. Selected metal elements of the monitored component of the composite material sample.

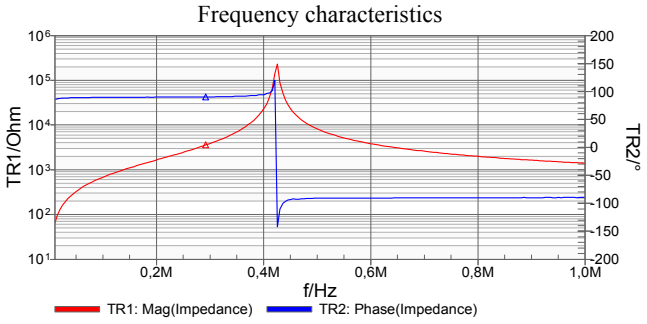

Fig.6. The frequency characteristics of the magnetic yoke: the resonant frequency of f_r=425.000 kHz.

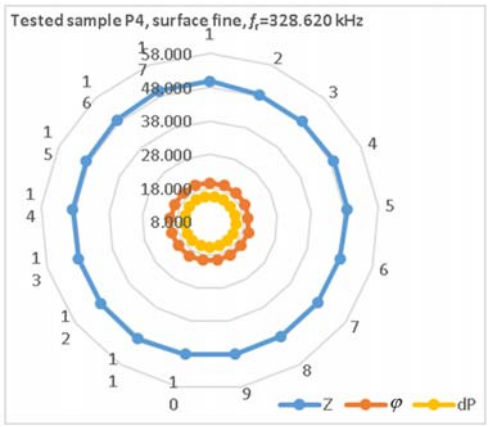

Fig.7. The measurement and evaluation of the impedance module/phase of the monitored component P4, impedance module Z, f_r=328.630 kHz: the fine surface, coarseness rate of Δx_{fi}<0.2 mm.

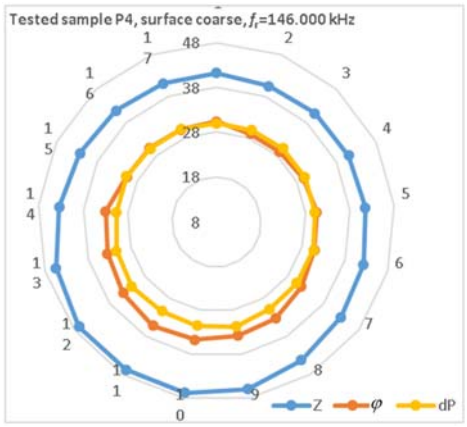

Fig.10. The measurement and evaluation of the impedance module/phase of the monitored component P4, impedance module Z, f_r=146.000 kHz: the coarse surface, coarseness rate of $\Delta x_{co}\cong$10 mm.

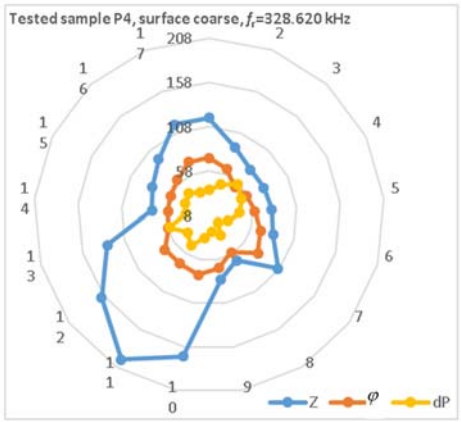

Fig.8. The measurement and evaluation of the impedance module/phase of the monitored component P4, impedance module Z, f_r=328.630 kHz: the coarse surface, coarseness rate of $\Delta x_{co}\cong$10 mm.

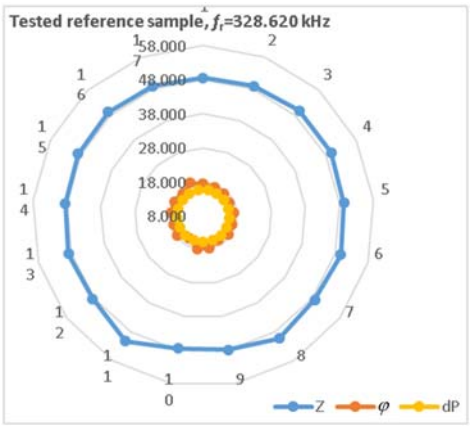

Fig.11. The measurement and evaluation of the impedance module/phase of the monitored component without the metal element, impedance module Z, f_r=328.620 kHz.

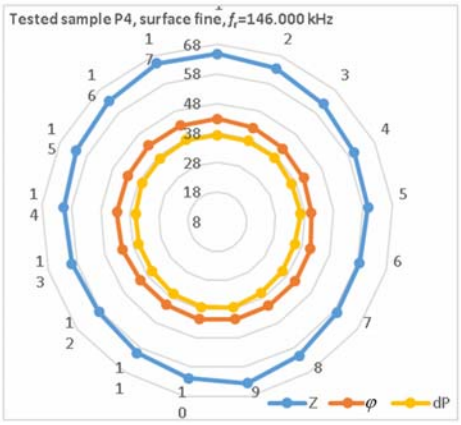

Fig.9. The measurement and evaluation of the impedance module/phase of the monitored component P4, impedance module Z, f_r=146.000 kHz: the fine surface, coarseness rate of Δx_{fi}<0.2 mm.

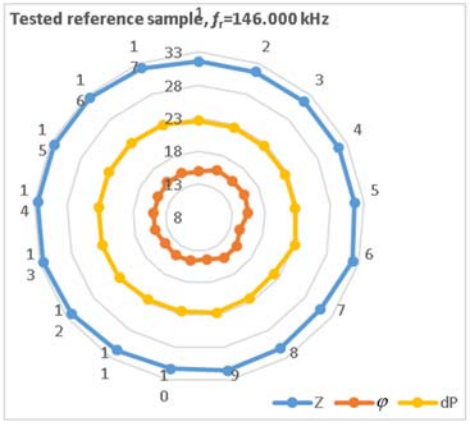

Fig.12. The measurement and evaluation of the impedance module/phase of the monitored component without the metal element, impedance module Z, f_r=146.000 kHz.

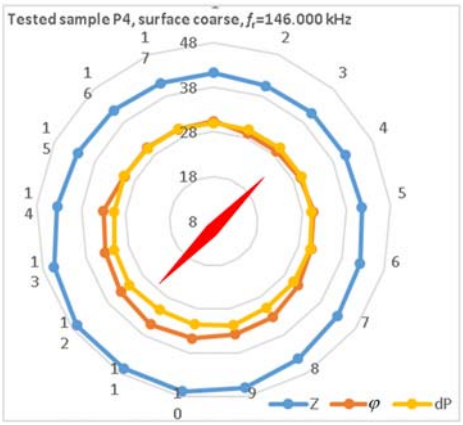

Fig.13. The measurement and evaluation of the impedance module/phase; a part of the composite orientation (red) in the monitored component P4, impedance module Z, f_r=146.000 kHz: the coarse surface, coarseness rate of $\Delta x_{co} \cong 10$ mm.

4. RESULTS

The results obtained from the blocks with the tested and evaluated distribution (homogeneity) of the composite material components, Fig.5., were analyzed for the frequencies of f_{r1}=3.450 kHz, f_{r2}=21.900 kHz, f_{r3}=50.120 kHz, f_{r4}=146.000 kHz, and f_{r5}=328.630 kHz. These frequencies had been preset to facilitate the evaluation of the dissipated power dP and, subsequently, the volumetric mass density ρ of the monitored metal elements. Using a simple test, we determined the volumes V_i, i=1,..,5 actively influenced by the magnetic field generated by the magnetic yoke (Fig.1.). In evaluating the volumetric mass density ρ, it is possible to further utilize the already assessed volumes $V_5 \cong 75$ cm^3, $V_4 \cong 375$ cm^3, $V_3 \cong 600$ cm^3, $V_2 \cong 900$ cm^3, and $V_1 \cong 1125$ cm^3. The coefficient k_V is then instrumental towards establishing the measured density of the metal composite ρ_{sam}; in this context, we assume steel exhibiting the specific electric conductivity and volumetric mass density of γ=9.93 MS/m and ρ_{Fe}, respectively.

The resulting volumetric mass density of the tested sample corresponds to

$$\rho_{sam} = \rho_{Fe} k_V \,. \tag{9}$$

We then employ the above formula (7) to express the content coefficient of the monitored composite component, from which the volumetric mass density ρ is enumerated.

The density coefficient of the monitored composite component corresponds to

$$k_V = \frac{4\pi\left(dP - dP_{fant}\right)}{U^2} Z_{v,Re}\,, \tag{10}$$

where dP_{fant} is the previously measured and evaluated magnitude of the dissipated power of the reference structure without the monitored composite. For the sample P4 at the depth of down to 10 mm from the surface, we then have $\rho_{P4,f,10mm}$ = 87.2 kg/m^3 from the fine side and **$\rho_{P4,co,10mm}$ = -135 kg/m^3** from the coarse side. A similar analysis can be performed for the depth of 50 mm, with $\rho_{P4,f,50mm}$ = 61.4 kg/m^3 and $\rho_{P4,co,50mm}$ = 27.6 kg/m^3 from the fine and coarse sides, respectively.

5. DISCUSSION

The measurement results presented within the previous chapter can be characterized and commented upon as follows:

1. It is invariably advisable to consider the analyses from the perspective of the reference sample, namely, the sample where the composite component has been eliminated (as characterized above in the form of the parameter dP_{fant}).
2. Fig.7. to Fig.12. can be used to interpret the inhomogeneities in the distribution of the monitored composite component, and these are then evaluable from the components of the modulus of the impedance Z, phase φ, and dissipated power dP in the graphical embodiment of the radial interpretation of the quantities.
3. Analyses where the properties of the tested sample are assessed at different depths have to assume the parameters of the electromagnetic field. As already indicated within related sections of the text, the low-quality surface finishes (namely, the highly coarse ones) exhibit – considering analyses down to 10 mm – a major difference between the evaluated density rates in the monitored composite component; this effect becomes obvious if we compare the parameters and graphs from Fig.7., Fig.8. and active losses dP_{co}= 39.1 μW, dP_{fi}=37.0 mW. The data differ to such an extent that, considering the technology applied to produce the sample, they can be regarded as inadequate values. The claim is verifiable via performing a measurement cycle in greater depths, for example, down to 50 mm below the surface; the data obtained for the depths of 10 mm and 50 mm differ fundamentally. An identical reference sample is characterized by the losses of dP_{co}=30.6 mW, dP_{fi}=36.6 mW, namely, values corresponding to the applied technology for fabricating the tested sample.
4. The evaluation of the density of the metal elements, namely, the monitored composite component, is derived from the dissipated power dP in the assumed space to be observed having volume V. In an inappropriately preset measurement cycle (or one where the low quality sample surface finish exhibits high roughness), including the influence of the remaining composite components in the form of dissipated power, dP_{fant}, will result in erroneous data on the volumetric mass density of the material of the component. Within our exemplary measurement, the information corresponding to such a condition is **$\rho_{P4,co,10mm}$ = -135 kg/m^3**, a value that points to inappropriate setting of the measurement and analysis of the sample.

6. CONCLUSION

We designed and tested a novel methodology using impedance in the complex form to facilitate NDT-based

measurement and evaluation of composite material components.

Test samples of composite materials with needle-like formations applied as the reinforcement were experimentally measured in laboratory conditions; in this context, we proved the basic functional principles of the designed NDT methodology for evaluating the distribution, density, and orientation of ferromagnetic/non-ferromagnetic conductive fibers in a composite material.

This novel metrological approach towards the NDT of composite materials exploits impedance analysis; the selected resonant frequency enables us to evaluate the quality of the examined composite at different depths below the surface of the given block sample.

The single-purpose devices designed and tested to support the NDT methodology exhibited sufficient sensitivity to evaluate the monitored components.

The outcomes of the measurement and evaluation of the fibers' directions and density are presented in chapters 3 and 4 above. Without major corrections, we evaluated the density (mass) of the steel fibers, which exhibited specific distribution density values at particular subsurface depths. The procedure proved to be valid and advantageous for use at frequencies within the band close to the resonance of the monitored region of the material.

Further research in the presented context will focus on verifying the accuracy of the volumetric mass density evaluation in the monitored composite material components.

ACKNOWLEDGEMENT

The research described herein was funded by the National Sustainability Program under grant No. LO1401. For the actual analyses and experiments, the infrastructure of the SIX Center was used.

REFERENCES

[1] Fiala, P., Friedl, M., Hobst, L., Komarkova, T. (2014). *Method of evaluating distribution, density and orientation of ferromagnetic electrically conducting fibers within composite material and detection device for making the same*. Czech Patent Application PV2014-742.

[2] Wang, W., Dai, Y., Zhang, C., Gao, X., Zhao, M. (2016). Micromechanical modeling of fiber-reinforced composites with statistically equivalent random fiber distribution. *Materials*, 9 (8), E624.

[3] Giasin, K., Ayvar-Soberanis, S. (2016). Evaluation of workpiece temperature during drilling of GLARE fiber metal laminates using infrared techniques: Effect of cutting parameters, fiber orientation and spray mist application. *Materials*, 9 (8), E622.

[4] Zou, S., Wan, Z., Lu, L., Tang, Y. (2016). Experimental study on tensile properties of a novel porous metal fiber/powder sintered composite sheet. *Materials*, 9 (9), E712.

[5] Mizukami, K., Mizutani, Y., Kimura, K., Sato, A., Todoroki, A., Suzuki, Y. (2016). Detection of in-plane fiber waviness in cross-ply CFRP laminates using layer selectable eddy current method. *Composites Part A: Applied Science and Manufacturing*, 82, 108-118.

[6] Zheng, K., Chang, Y.S., Wang, K.H., Yao, Y. (2016). Thermographic clustering analysis for defect detection in CFRP structures. *Polymer Testing*, 49, 73-81.

[7] Santoro, S., Drioli, E., Figoli, A. (2016). Development of novel ECTFE coated PP composite hollow-fiber membranes. *Coating*, 6 (3), 40.

[8] Martinie, L., Roussel, N. (2011). Simple tools for fiber orientation prediction in industrial practice. *Cement and Concrete Research*, 41 (10), 993-1000.

[9] Shah, A.A., Ribakov, Y. (2011). Recent trends in steel fibered high-strength concrete. *Materials and Design*, 32 (8-9), 4122-4151.

[10] Ozyurt, N., Mason, T.O., Shah, S.P. (2006). Non-destructive monitoring of fiber orientation using AC-IS: An industrial-scale application. *Cement and Concrete Research*, 36 (9), 1653-1660.

[11] Szymanik, B., Frankowski, P.K., Chady, T., Azariah, C.R., Szczecin, J.C. (2015). Detection and inspection of steel bars in reinforced concrete structures using active infrared thermography with microwave excitation and eddy current. *Sensors*, 16 (2), 234.

[12] Hobst, L., Bílek, P., Vodička, J., Vala, J. (2014). Measurement of set fibre-concrete homogeneity in finished steel fibre-concrete structure of segmental tunnel lining. *Advanced Materials Research*, 1106, 41-44.

[13] Fiala, P., Friedl, M., Hobst, L., Komarkova, T. (2015). *A method and a detection device for evaluating the distribution, density and orientation of ferromagnetic, electrically conductive fibres in a composite material*. International Patent Application PCT/CZ2015/000132, publ. no. WO 2016070859 A1.

Received November 15, 2017.
Accepted February 20, 2018.